FABRICATION AND CORROSION ASSESSMENT OF BIODEGRADABLE METALLIC ALLOYS FOR PATIENT-SPECIFIC BONE IMPLANT APPLICATIONS

By

Austin Sims

Hamdy Ibrahim
Assistant Professor of Mechanical Engineering
(Chair)

Louie Elliott
Assistant Professor of
Mechanical Engineering
(Committee Member)

Mohammad Mahtabi
Assistant Professor of Mechanical Engineering
(Committee Member)

FABRICATION AND CORROSION ASSESSMENT OF BIODEGRADABLE METALLIC ALLOYS FOR PATIENT-SPECIFIC BONE IMPLANT APPLICATIONS

By

Austin Sims

A Thesis Submitted to the Faculty of the University of Tennessee at Chattanooga in Partial Fulfillment of the Requirements of the Degree of Master of Science: Engineering

The University of Tennessee at Chattanooga
Chattanooga, Tennessee

May 2021

ABSTRACT

Biodegradable metals and alloys are materials that are intended to remain in the body long enough for healing to occur, and then degrade or dissolve after their service lifetime. Permanent implants are often much stiffer than the bone they are supporting, which can lead to loss of bone density, mechanical failure of the implant, and require corrective surgery. Biodegradable orthopedic implants offer strength and stiffness close to that of bone, prevent the need for corrective surgery, and eliminate the long-term existence of a foreign object in the body. In this work, in vitro corrosion of magnesium-samarium(III) oxide nanocomposites are studied for their use as biodegradable orthopedic materials. The Mg-1%Sm_2O_3 nanocomposite shows a promising corrosion rate, lower than pure magnesium. Additive manufacturing of zinc paste is also explored as a medium for fabrication of patient-specific implants. This work provides insight into the development of magnesium-based nanocomposites as biodegradable materials.

DEDICATION

This work is dedicated to my parents, who have made many sacrifices to provide the resources and opportunities necessary for developing the knowledge and skills I have today. Their capacity for love and encouragement truly has no limit.

ACKNOWLEDGEMENTS

I would like to thank Dr. Hamdy Ibrahim for entrusting me with the development of his existing work, and for his continued support and guidance throughout this process. He has sacrificed a significant amount of his time and resources to allow me to pursue my passions, and for that I am grateful. I would like to thank Dr. Louie Elliott for his wisdom and assistance throughout my academic career at UTC, and especially during my additive manufacturing obstacles. I would like to thank Dr. Trevor Elliott for providing the opportunity for me to work as a graduate assistant. I would like to thank Moataz Abdalla for his work and support throughout our time as lab partners. I would like to thank Karl Fletcher for his help setting up our lab. I would also like to thank Ben Swords for his assistance in fabricating the nanocomposite samples.

TABLE OF CONTENTS

LIST OF TABLES

LIST OF FIGURES

LIST OF ABBREVIATIONS

3-D, Three-Dimensional

A, ampere

A, original surface area

AC, alternating current

CAD, Computer Aided Design

cm, centimeter

cm^2, square centimeter

cm^3, cubic centimeter

CPE, constant phase element

CR, Corrosion Rate

CR, corrosion rate

D, diameter

DC, direct current

e^-, electron

E, potential (volts)

EIS, Electrochemical Impedance Spectroscopy

EW, equivalent weight

F, farad (capacitance)

g, gram

GHz, Gigahertz

h, height

h, hour

HEC, hydroxyethyl cellulose

HEPES, 4-(2-hydroxyethyl)-1-piperazineethanesulfonic acid (buffering agent)

Hz, hertz

K, kelvin

ksi, kilo pound per square inch

L, length

m, mass

m^3, cubic meter

Micro-CT, micro-Computed Tomography

min, minute

mL, milliliter

mm, millimeter

mol, mole

MPa, Mega pascal

m-SBF, modified Simulated Body Fluid

mV, millivolts

n, number of moles

nm, nanometer

OCP, open circuit potential

P, pressure

Pa, pascal

PDP, Potentiodynamic Polarization

pH, potential of hydrogen

ppm, parts per million

PVA, polyvinyl alcohol

REE, Rare Earth Elements

s, seconds

SBF, Simulated body fluid

SEM, Scanning Electron Microscope

Sm_2O_3, samarium(III) oxide

t, exposure time

T, immersion time

UTS, Ultimate Tensile Strength

V, volume

W, mass loss

W, watt

Wt%, weight percent

Z, number of atoms or molecules per unit cell

LIST OF SYMBOLS

µA, microampere

µm, micrometer

ºC, degrees Celsius

a_i, atomic weight of element i

B, proportionality constant

$E_{corr,}$ corrosion potential

f_i, mass fraction of element i

i_{corr}, corrosion current

I_{corr}, corrosion current density

M_w, molecular weight

N_A, Avogadro's number

n_i, number of valence electrons of element i

Q_c, capacitance of corrosion products layer

Q_{dl}, capacitance of double layer

R_p, polarization resistance

R_s, solution resistance

R_t, charge transfer resistance

V_c, unit cell volume

β_A/Beta A/b_a, anodic reaction from Tafel data

β_c/Beta C/b_c, cathodic reaction from Tafel data

ΔW, weight loss

ρ, density

$\rho_{measured,avg}$, average measured density

$\rho_{theoretical}$, theoretical density

Ω, ohm

CHAPTER I

INTRODUCTION AND BACKGROUND

The utilization of biomaterials for medical applications has gained significant interest recently. Budgetary constraints on medical care have led to an increased necessity for efficient treatment and preventative techniques. Traditionally, inert metallic alloys such as Ti-6Al-4V (surgical grade 5 titanium), have been used for holding fractured bone together permanently [1]. The use of permanent implants is associated with problems such as stress shielding, inflammation, and incomplete tissue healing, often requiring a second implant removal surgery [2]. Implant removal surgery is both costly and time consuming for medical institutions and/or patients, so the study of non-permanent biomaterials is essential to the progress of surgical implantation practices.

Biodegradable metals and their alloys have gained attention because of their numerous advantages over conventional inert metals and more recent biodegradable polymer compounds [3]. Magnesium and zinc-based alloys are particularly useful when considering orthopedic applications [4]. The most obvious advantage of magnesium and zinc is their excellent biocompatibility. When alloyed, their mechanical strengths and moduli can closely match that of desired bones. This is especially important for orthopedic use because implants that bear too much load will result in decreased bone density, known as stress shielding [5]. On the other end of the spectrum are polymer implants. Self-dissolving sutures have been widely used throughout the medical field for years, and biodegradable screws and pins have recently been developed from polymers [6]. However, higher strength is required for many orthopedic applications, and metallic implants possess a clear advantage over biodegradable polymers [7]. Bone fixtures and bone scaffolds are the primary areas of research for metals in orthopedic applications [5]. This work focuses on the development of materials for bone fixtures.

Every case of bone trauma is different and the use of a standard implant for every patient, the current treatment methodology, results in suboptimal healing outcomes. The idea of using patient-specific implants is one way to produce better clinical results. Additive manufacturing (3-D printing) is currently the most feasible method for producing a specific implant designed for each patient. Because of biocompatible metals' reactivity and high melting point, typical extrusion-type printing is extremely difficult. However, the geometry formation and bonding can be separated into two steps by using methods such as binder-jet or paste extrusion printing coupled with post processing. Binder-jet printers use an adhesive to bond the metal powder together and form a part. Paste extrusion utilizes a suspension of metal particles in a viscous medium to form a part via extrusion. Both methods result in a part generated without forcing the metal through a phase change. Heat treatment is then used to remove the adhesive binder and melt the metal particles into a bulk part. In this research, paste extrusion of zinc is explored as a method for fabricating biodegradable metallic implants.

The most crucial property of biodegradable materials is their controlled degradation. Materials that degrade too quickly can result in toxicity and premature implant failure [2]. Incorporation of nanoparticles into the matrix of a metal or alloy (nanocomposites) has the capability to increase its mechanical properties and corrosion resistance. In addition to the work on the extrusion of zinc, this thesis presents a study on the in vitro corrosion behavior of fabricated magnesium-samarium(III) oxide nanocomposites for biodegradable orthopedic use. A medium simulating the physiological environment, namely a modified simulated body fluid (m-SBF), is used to assess these promising nanocomposites' corrosion behavior. These results provide a framework for the development of biodegradable magnesium-based nanocomposites.

The primary objective of this work is to develop a paste for additively manufacturing reactive metals to generate biodegradable orthopedic implants which are designed for individual patients. The secondary objective of this work is to quantify the corrosion rates of magnesium-samarium(III) oxide nanocomposites to determine their feasibility as biomaterials.

This work begins with a review of magnesium and zinc as biomaterials, additive manufacturing techniques, and corrosion testing techniques. Pure zinc powder was blended with different ratios of aqueous hydroxyethyl cellulose and polyvinyl alcohol solutions to develop a paste for extrusion printing. A paste containing zinc and polyvinyl alcohol was unachievable with available equipment because of flocculation. A paste containing 75% zinc and 25% hydroxyethyl cellulose solution (4% HEC, 96% DI water) was manually extruded to visually observe viscosity and layer adhesion. Further samples of zinc/HEC paste were cast at varied ratios and heat treated. Corrosion rates of magnesium-samarium(III) oxide nanocomposites at three compositions were also found via PDP, EIS and Immersion testing. The corrosion rate of pure magnesium was used as a baseline comparison for the nanocomposites.

CHAPTER II

LITERATURE REVIEW

Magnesium as a Biodegradable Material

Magnesium is an essential mineral to the human body, especially when concerned with metabolism and osteogenesis (the formation of bone) [8]. The majority of magnesium, over half of the total content, in the body is found in bones [9]. Previous work has shown the relationship between magnesium and bone growth, making it an interesting candidate for the biodegradable orthopedic implant field [10, 11]. The small intestine is the primary organ responsible for absorbing magnesium, with renal absorption playing a part, and excess is excreted through urine. Additionally, homeostasis is achieved over a large range of dietary intake of magnesium through these absorption and excretion methods [11].

Dissolution of magnesium in aqueous solutions results in hydrogen evolution [12]. Higher degradation rates result in an excessive amount of hydrogen gas at the implantation site, which can form gas cavities. Gas cavities with enough hydrogen gas create pressure, adding unwanted stress to the implant, and cause an imbalance in blood cell parameters [13]. Pure magnesium has a preferable lower degradation rate than magnesium alloys, so purification techniques are some of the main areas of development for magnesium implants. Pure magnesium also has a relatively low elastic modulus when compared to load-bearing implants. However, its use for non-load-bearing applications, such as screws, has been studied [14]. Magnesium alloys can reach elastic moduli close to that of human bone. This allows load transfer from the implant to the surrounding bone during healing and prevents stress shielding [15].

Current biodegradable orthopedic implants are made of polymers, which have lower strength and do not promote bone growth. Magnesium-based alloys have higher strength and have been shown to significantly increase the mineralized bone area and formation of new bone, compared to polymer implants, when tested in vivo [7].

In Vitro and In Vivo Degradation of Magnesium

To fully understand the practicality of biodegradable magnesium bone implants, the degradation mechanism must be considered. Magnesium and magnesium alloys degrade in aqueous environments through a corrosion process. This is an electrochemical process which forms magnesium hydroxide and hydrogen gas. The corrosion reaction is shown below:

$$Mg_{(s)} + 2H_2O_{(aq)} \rightleftarrows Mg(OH)_{2\,(s)} + H_{2\,(g)} \quad (1)$$

As the reaction begins, a protective layer of magnesium hydroxide $Mg(OH)_2$ forms on the surface. This is the primary reason magnesium has an increased degradation rate initially, and then slows as the reaction continues. However, biological environments contain chloride ions, which react with the magnesium hydroxide layer to form magnesium chloride [16]. Since magnesium chloride is highly soluble, the protective layer begins to degrade, and pitting corrosion ensues. As the corrosion rate of magnesium increases, hydrogen evolution begins to increase as well. This increases the potential for hydrogen gas cavities to form in vivo, which can cause inflammation, tissue damage, and premature failure of the implant [17].

In vitro studies of magnesium are mainly performed with electrolytic simulated body fluid (SBF) or modified simulated body fluid (m-SBF), with the most common solution being Hank's solution [18-22]. Methods for corrosion testing can be divided into two categories, polarized and unpolarized. The distinction between the two is that polarized experiments utilize a driving force, which is applied or measured during the experiment [23]. Electrochemical Impedance Spectroscopy (EIS) and Potentiodynamic Polarization (PDP) are examples of polarized experiments, and immersion testing [24] constitutes the prominent unpolarized method. Further explanation of in vitro testing is given in subsequent sections.

In vivo studies are commonly conducted with rats, guinea pigs, or rabbits. Ideally, animal models are created alongside in vivo experiments to strengthen the relationship between simulations and real physiological environments. This is important because the investigation of in vivo degradation and biocompatibility requires long-term study, and robust models could reduce the amount of time spent designing optimal implantation hardware.

In vivo studies are useful for study of bone, tissue, and blood responses to certain magnesium purity and/or alloy systems [25]. Follow-up testing methods such as micro-CT, serum analysis, radiographic examination, and implant examination can be used to characterize local reactions to implantation [26]. Degradation rate, stability of the material, and corrosion products will play a part in the local response to an implant [27]. Corrosion rates are measured based on either weight loss or volume loss. Weight loss is calculated ex vivo, that is, after the implant is removed. The corrosion rate can be found using the following equation:

$$CR = 8.76 \times 10^4 \Delta W / A t \rho \ , \tag{2}$$

where ΔW: weight loss (g), A: original surface area (cm^2), t: exposure time (days), and ρ: standard density of the material (g/cm^3) [28]. Corrosion rates based on volume loss can be calculated directly, using volume loss of the actual implant, or indirectly, using the volume of hydrogen evolution. Three dimensional micro-CT images are used to calculate the direct volume loss of an implant with:

$$CR = 8.76 \times 10^4 \Delta V/At\ , \quad (3)$$

where ΔV: differences in volume before-after immersion (cm^3), A: original surface area (cm^2), and t: exposure time (days) [26]. The volume measurement for hydrogen evolution is performed ex vivo, and is calculated using the ideal gas law:

$$PV = nRT\ , \quad (4)$$

where P: standard atmospheric pressure (Pa), V: volume of H_2 (m^3), n: substance amount of the gas (mol), and T: temperature (K) [26]. To date, a correlation between in vitro and in vivo degradation has not been well established [29, 30]. However, Hofstetter et al [31] found that ultrahigh-purity magnesium (iron impurities of 0.2-2.2 ppm) exhibited close in vitro and in vivo degradation rates of approximately 10μm per year. While it is difficult to determine the relationship between in vitro and in vivo studies, further experimentation will lead to more data available for mathematical interpretation. However, in vivo testing is not explored in this study.

Magnesium Alloys

Although pure magnesium has promising biocompatibility, manufacturing high purity magnesium is difficult, and its mechanical properties are suboptimal for most orthopedic applications. This has led to the development of magnesium-based alloys. Common alloying elements for magnesium include aluminum, zinc, and rare earth elements. Mg-Al alloys have moderate mechanical properties, and excellent castability and corrosion resistance. Furthermore, an increase in aluminum content results in significant improvement of the alloy's corrosion resistance, due to the formation of an aluminum oxide film [32]. It should be noted that aluminum is a well-known neurotoxicant, so the content in these alloys must be limited to keep the aluminum release below established weekly intake limits [33].

Mg-Zn alloys are known for having excellent biocompatibility, since zinc is an essential element in the human body. Mg-Zn alloys also have improved mechanical properties compared to pure magnesium. The addition of rare earth elements to Mg-Zn alloys has shown an increase in mechanical

properties and corrosion resistance. A more in-depth discussion of zinc as a biodegradable material is given in subsequent sections.

Rare earth elements (REE) are typically used in alloy systems with various elemental compositions. This allows for a wide range of mechanical and corrosion characteristics, further extending the applications of biodegradable materials. Potential alloying REE's include Y, Gd, Tb, Dy, Ho, Er, Tm, Yb, Lu, Nd, La, Ce, Pr, Sm, and Eu [34]. A recent in vitro study of Mg-REEs has shown that Y, La, Ce, and Pr are most compatible with orthopedic applications, while Sc, Nd, Sm, Eu, Gd, Tb, Tm, and Yb have shown better compatibility with cardiovascular applications [35]. Since these alloying systems often contain more than one REE, it is difficult to consider the influence of these combinations in practice due to lack of impurity and cellular interaction analysis [36].

Controlling Degradation Rates with Surface Modification

Although magnesium and its alloys have favorable properties as biodegradable metals, the degradation itself is fast and difficult to control. Rapid degradation of magnesium implants can result in premature loss of mechanical properties, hydrogen bubbles, bone absorption, and hemolysis [37]. An effective way to control the degradation of magnesium, as well as other biodegradable metals, is surface modification. Using biocompatible coatings is the most common surface modification process, where a coating layer is created on the surface of the implant. This layer shields the underlying metal to delay its corrosion. Coatings for implants must be biocompatible and bioactive to prevent toxicity and degrade in a controlled manner. Anodization, microarc oxidation, ion implantation, and chemical conversion coatings are common examples of surface modification techniques [38]. Surface modification is not explored in this study. However, Yin et al [39] has reviewed advances in biodegradable surface coatings.

Magnesium Nanocomposites

While magnesium and its alloys have compatible properties for biomedical applications, they suffer from limitations of mechanical properties and degradation rates. Nanocomposites have the ability to improve properties such as strength, ductility, and corrosion resistance of biodegradable materials [40]. Because of this, they have gained popularity as research materials for clinical applications. Nanocomposites are produced by embedding nano-sized reinforcements into a metal matrix. Powder metallurgy is a common manufacturing method because the particles can be blended in an alloy system and then post processed to desired properties [41]. Rare-earth element nanoparticles, specifically rare-earth oxide nanoparticles, have been studied as reinforcements to increase the strength of the magnesium matrix and its grain refinement. Robinson et al. [42] found that an annealed Mg-Nd alloy showed no significant grain boundary segregation after recrystallization. Studies of Mg-Y_2O_3 [43] and Mg-Sm_2O_3 [44] have resulted in increased grain refinement, hardness, strength compared to magnesium.

Magnesium nanocomposites have also been fabricated using non-metal reinforcements. Biocompatibility is often a concern when utilizing rare-earth elements for biomedical applications, even though they possess higher mechanical properties. Non-metal reinforcements offer better biocompatibility and mechanical properties suitable for low load-bearing applications, however. Parai et al. [45] studied the effect of Mg-Ca-Zn nano-composite foams reinforced with nano-hydroxyapatite to produce porous scaffolds. Improvement of compressive strength and Young's modulus was reported, with mechanical properties in the range of cancellous bone. Addition of hydroxyapatite is expected to enhance new bone tissue regeneration, but in vitro studies are still being conducted. A magnesium-fluorapatite nanocomposite improves mechanical properties, reduce corrosion rate, and accelerate the formation of an apatite surface layer, which helps protect the metal matrix during degradation [46].

Zinc as a Biodegradable Material

Zinc, like magnesium, is an essential element in the human body. It is also one of the most abundant nutritional elements, found in all body tissues. Muscle and bone contain most of the bodily zinc, comprising 85% of the total zinc content [47]. Zinc is also known to be essential for over 300 enzymic reactions and a large number of macromolecules' structure and functions. Unlike magnesium, the mechanisms for zinc homeostasis are not well known [48]. Plum et al. [49] found that excess zinc is safely excreted through the kidneys. However, study of zinc homeostasis in rats has shown that absorption and excretion of zinc through the gastrointestinal tract is the primary method for regulation [50].

Degradation of pure zinc is not known to cause detrimental health effects. On the contrary, zinc has been shown to be a highly effective inhibiter of osteoclastic bone resorption when tested in vitro [51]. Zinc has an ideal corrosion rate for orthopedic applications of approximately 50 μm/year. It lies between magnesium, which has a high corrosion rate, and iron, which has a much lower corrosion rate [52]. This contributes to its biocompatibility since corrosion products are generated at a low rate. However, pure zinc has poor mechanical properties compared to other metals. A popular method for improving zinc's mechanical properties is fabricating Zn-based alloys—thus making it possible for zinc alloys to possess superior strength and ductility compared to some magnesium alloys [53].

In Vitro and In Vivo Degradation of Zinc

When considering zinc as a biodegradable orthopedic material, the degradation mechanism is possibly its most impressive quality. Most notably, zinc does not produce hydrogen gas during corrosion, unlike magnesium [54-56]. Zinc and its alloys corrode in aqueous solutions generally through anodic and cathodic reactions when pH is around 7.4, or near neutral conditions. The corrosion reaction is shown below as:

$$\text{Anodic: } Zn \rightarrow Zn^{2+} + 2e^{-} \quad (5)$$

$$\text{Cathodic: } O_2 + 2H_2O + 4e^{-} \rightarrow 4OH^{-} \quad (6)$$

$$Z\text{inc Hydroxide: } Zn^{2+} + 2OH^{-} \rightarrow Zn(OH)_2 \quad (7)$$

$$\text{Zinc Oxide: } Zn(OH)_2 \rightarrow ZnO + H_2O \quad (8)$$

Electrons generated during the anodic reaction are consumed during the cathodic reaction, while zinc hydroxide and zinc oxide reactions occur on the surface of the implant. The presence of chloride ions in body fluid dissolves zinc hydroxide and zinc oxide products, which exposes the zinc substrate to the solution. This encourages continuous cycles of anodic and cathodic reactions [57]. The primary cathodic reaction of zinc is driven by oxygen reduction. Hydroxyl ions and metal ions released during degradation cause an increase in local pH, which results in precipitation of the oxides and hydroxides. However, solubility products are formed at a much lower rate than those of magnesium, so the periods of dissolution and absorption are longer for zinc [58].

In vitro studies of zinc are performed in the same manner as other biodegradable metals, which are discussed in previous and subsequent sections. Experiments are conducted in a simulated body fluid or modified simulated body fluid, and either polarized or unpolarized tests are conducted. Polarized experiments are most useful for determining corrosion mechanism data, such as zinc ion concentration. Unpolarized experiments, such as immersion testing, are popular for gathering corrosion rate data.

In vivo studies are important for determining the physiological compatibility of biodegradable materials. Local tissue and blood samples may be examined for inflammatory, immune, bone ingrowth, etc., responses to an implant. Of course, corrosion rate determination under true physiological conditions is a distinct benefit of in vivo testing as well. Corrosion rates are typically determined based on mass or volume loss, similar to the method described for magnesium. However, corrosion rates based on hydrogen evolution do not pertain to zinc degradation. An early study of pure zinc wires implanted into the abdominal aortas of adult rats resulted in no negative tissue effects or toxicity after 6 months [54]. A more recent study of pure zinc stents implanted into abdominal aortas of adult rabbits resulted in no toxicity or corrosion product accumulation after 12 months, although slight inflammation was observed [56]. While in vitro and in vivo studies have confirmed the biocompatibility of zinc, its mechanical properties remain a common issue. To overcome this obstacle, study of the mechanical properties of zinc and its alloys will extend their usefulness as biodegradable orthopedic materials.

Zinc Alloys

Zinc-based alloys have gained popularity because of pure zinc's excellent biocompatibility and its need for improved mechanical properties. Pure zinc may be suitable for some low load-bearing applications, but zinc alloys are necessary to provide ideal mechanical properties for orthopedic applications requiring higher strength. Currently studied alloying elements for zinc include Mg, Ca, Sr, Al, Cu, Li, and Mn. The most obvious choice of biodegradable alloys for orthopedic use is Zn-Mg alloys because both elements are known for their biocompatibility. Zn-Mg alloys can achieve high strength with corrosion rates comparable to pure zinc. Vojtech et al. [59] found that a Zn-1Mg alloy achieved an Ultimate Tensile Strength (UTS) of around 150 MPa, compared to tensile strength of bone at 30-280 MPa, and a corrosion rate nearly matching pure zinc at pH's of 5,7 and 10.

Alloying of zinc with elements other than magnesium have resulted in superior mechanical and corrosion properties. Addition of Al and Cu to these alloying systems is often omitted because of the detrimental health effects surrounding aluminum and copper. Publications, albeit a limited amount, of Zn alloys have mainly focused on addition of Li, Ca, and Sr. One study of an extruded Zn-0.4Li alloy resulted in a maximum tensile strength up to 520 MPa and a corrosion rate around 20μm/year [58]. This is significantly stronger than the tensile strength of bone (30-280 MPa) and about one half the corrosion rate of pure zinc. Another study on zinc alloys found that an extruded Zn-1Ca alloy resulted in a tensile strength of approximately 200 MPa and a corrosion rate approximately 10% higher than pure zinc [24]. The same study found that an extruded Zn-1Sr alloy resulted in a tensile strength of approximately 220 MPa with a corrosion rate approximately 20% higher than pure zinc [52]. The current outlook of zinc alloys for orthopedic use is promising, and further study of alloying systems may prove zinc as the primary element for use in biodegradable metal implants.

Additive Manufacturing of Biodegradable Metals

Additive manufacturing refers to the process of building a three-dimensional object by joining layers of material on top of one another. The path for building these objects is drawn using computer-aided-design (CAD), which is sliced into two-dimensional layers. Additive manufacturing is typically classified into seven main categories: powder-bed fusion, directed energy deposition, sheet lamination, material extrusion, binder jetting, material jetting, and vat photopolymerization. Powder-bed fusion and binder jetting are the most popular methods for additive manufacturing of metals.

Magnesium and Zinc present a special processing challenge because of their chemical reactivity and evaporation products. Powder Bed Fusion is difficult because evaporation products can impede propagation of the energy source [60]. Binder jetting is the most promising method for additive manufacturing of biodegradable metals because the particles can be bound together at low temperatures and then heat treated in an inert atmosphere. Extrusion printing of metals also offers geometry formation at low temperatures paired with post processing in an inert atmosphere. Research on extrusion printing has been reported for nonbiodegradable metals [61, 62], but this method is still in an early stage of development.

Porosity control is often studied when additively manufacturing biodegradable implants because non-metal additives leave voids when removed during post processing and the remaining metal particles must properly bind to form a structure with proper porosity. Post processing parameters and metal powder properties are the most influential factors when fabricating porous scaffolds. Heating rate, final temperature, and holding time affect porosity when heat treating fabricated structures. Metal powder properties, such as shape, density, and size, determine how the particles will bind during fabrication and heat treatment. Gas atomization is generally the only feasible powder production process because it results in spherical powder with a minimum amount of oxygen. This is important because spherical powder is more uniform, and oxidation inhibits heat treatment of the fabricated parts.

Binder Jetting

Binder jetting is a powder-bed type of additive manufacturing that uses a liquid binder instead of thermal energy for binding. Powder is spread over a build platform and the printhead deposits a liquid binder over specified areas in each layer. The build platform lowers to allow each subsequent layer of powder to be deposited, spread evenly with a roller, and binder applied. Figure 1 shows a schematic of the process. Surrounding powder provides support for the structure during fabrication, so features such as large overhangs are possible with this method.

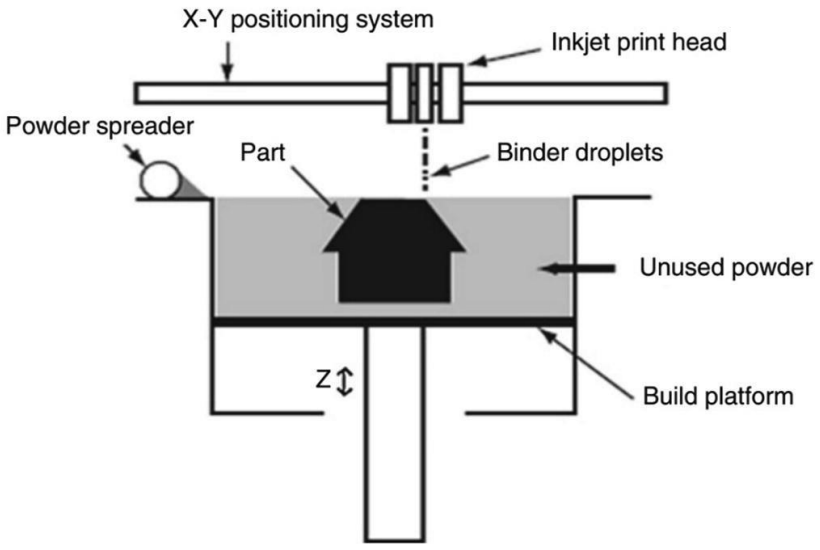

Figure 1

Schematic of a Binder Jetting Process, adopted from [63]

Extrusion

Extrusion printing of metal paste is similar to fused deposition modeling of thermoplastics. Instead of a roll of filament, metal powder is mixed with a binder to form a viscous paste. The paste is fed through an extruder using pressure from a piston or pump and deposited in specified areas of each cross section to form a 3-dimensional part. Evaporation of the binder's solvent provides higher quality layer adhesion during paste printing. Additionally, optimal viscosity is important for quality control and accuracy of fabricated parts [61]. Currently, the most significant advantage of extrusion printing is low equipment cost relative to other additive manufacturing methods for metal parts.

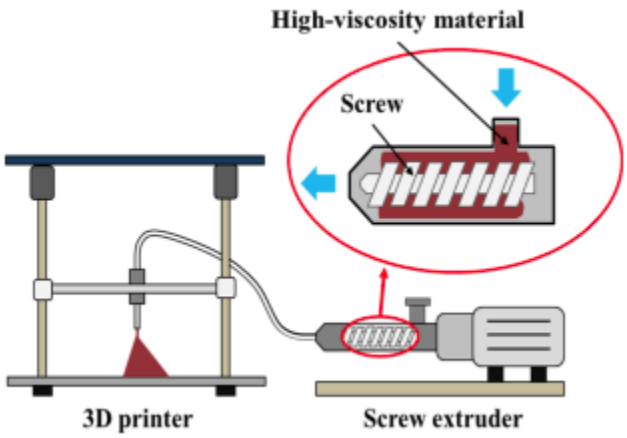

Figure 2

Schematic of an Extrusion Process Utilizing a Screw Extruder, adopted from [61]

Corrosion Testing Methods

Corrosion testing of biodegradable metals provides valuable information for determining how long a particular metal or alloy will remain in the body after implantation. Additionally, corrosion testing can be combined with mechanical testing to approximate the amount of time an implant will provide structural support during degradation. Immersion testing is particularly useful in this regard because samples can be removed at any point and tested for failure criteria. Electrochemical Impedance Spectroscopy and Potentiodynamic Polarization are popular electrochemical testing methods because they can provide yearly corrosion rate approximations while taking only minutes or hours to complete. Simulated body fluid (SBF) or modified simulated body fluid (m-SBF) is used as the solution for corrosion testing. Maintaining the pH of the solution at a specified value (pH 7.4), concentration of oxidizing ions, and fluid turbulence will provide higher quality results because the test more closely resembles in vivo conditions.

Electrochemical Impedance Spectroscopy

Electrochemical Impedance Spectroscopy (EIS) is a technique that uses the frequency response of AC polarization to provide surface data of a sample for degradation. A range of voltage frequencies is used to create a range of low magnitude polarizing voltages, which cycle from peak anodic to peak cathodic voltage. For each frequency, resistance and capacitance values are obtained. The resistance and capacitance values are used to define metal surface properties and interactions. In particular, EIS provides surface impedance data from a polarized sample. The impedance is used to resolve the dissolution rate of a sample, because it is directly proportional to corrosion resistance [64].

Since EIS is a non-destructive technique, the same sample can be used for multiple tests without the need for re-polishing. The formation of a corrosion or passivation layer is detected when EIS is performed over a long period of time, which shows the contribution of each layer to protection of the sample surface. Evaluation of coatings is performed in the same manner, which provides data for how long the coating will remain before breaking down. EIS does suffer from some limitations, however. Since the corrosion rate is not directly being measured, it does not account for degradation that occurs during the actual experiment. This extends to the corrosion rate changes that occur during experiments with alloys as well. One way to combat with this problem is to increase the measurement frequency so reactions during the test are more likely to be observed [23].

Potentiodynamic Polarization

Potentiodynamic Polarization (PDP) is an electrochemical technique that uses current flow between a working (the sample in question, such as Mg) and counter (inert metal) electrode to sweep voltage at a controlled rate. The open circuit potential (OCP) is determined prior to an experiment by allowing the sample to reach a steady potential. The OCP is required because the material needs to stabilize with the electrolyte before data collection begins. An initial (cathodic) voltage, below the OCP, is chosen and the voltage sweeps toward positive (anodic) values until the test is complete. Corrosion

potential is recorded as a function of corrosion current density to generate a polarization curve. Tafel extrapolation is commonly used with a polarization curve to find corrosion potential, corrosion current density, and corrosion rate values [23].

Unlike EIS testing, PDP is a lightly destructive testing technique. Samples can be used for multiple experiments, but they must be re-polished and cleaned to remove the corrosion damaged layer before performing further tests. Quantification of anodic and cathodic reaction rates over a range of potentials is possible through PDP testing. This is especially useful when studying the corrosion mechanisms of magnesium and its alloys because two alloys may have similar current densities but largely different corrosion potentials, due to anodic or cathodic kinetics. Underlying causes for change in corrosion may be determined based on the results. On the other hand, polarization curves for Mg are sensitive to preparation conditions [65]. Therefore, it is important to meticulously prepare a sample for testing, determine initial values, and interpret the extrapolation curve when studying corrosion characteristics of magnesium and its alloys.

Immersion Testing

Immersion testing is a non-polarizing technique for corrosion testing. Samples are immersed in either SBF or m-SBF solution and degrade without an applied current to accelerate the process. Changes in mass loss, pH, and hydrogen evolution can be used to determine corrosion rates for immersion tests. Time points for data collection, such as 5 days, 7 days, 14 days, etc., are determined prior to the test. Samples are removed at each time point to measure changes in mass and/or pH. Mass loss is the most common method for determining corrosion rates because data collection is simple, reliable, and does not require special equipment. Additionally, a corrosion rate calculation based on mass loss is straightforward, so errors associated with curve interpretation and initial values do not arise. Changes in pH are related to higher corrosion rates, and pH data is useful for understanding the corrosion behavior of magnesium and its alloys [66].

Immersion testing is a highly destructive technique for measuring corrosion, and samples are often unable to be reused after the experiment is completed. Longer immersion times provide more realistic results, so time constraints may limit the feasibility of immersion testing. Also, it is nearly impossible to replicate in vivo conditions at this point, so it is difficult to extend the evaluation of in vitro testing to in vivo applications because of experimental conditions and environmental effects of degradation [66]. However, immersion testing can provide more reliable data compared to accelerated electrochemical testing since configuration paired with extrapolation is not required and corrosion products do not skew data from mass loss.

CHAPTER III

METHODOLOGY

Pure Zinc

Zinc powder (8 μm, 99%, Pyro Chem Source) was used to synthesize a viscous metal paste. Hydroxyethyl cellulose (HEC; MakeYourOwn) and polyvinyl alcohol (PVA; EastChem) were used for viscosity enhancement and binder materials. All chemicals were stored in air-tight glassware to prevent oxidation and/or moisture absorption.

Synthesis of Zinc Metal Paste

Initial experimentation of metal powder/binder ratio was carried out based on previous work by Hong et al. [61]. HEC was dissolved in deionized water at wt% ranging from 1-5% to visually determine the optimal baseline for a binder gel. Similarly, PVA was dissolved in deionized water at wt% ranges from 1-20%. HEC at 4%wt showed the most promising thickness based on manual extrusion. PVA showed a problem with flocculation (clumping of particles) and did not transform into a gel at any of the tested ratios.

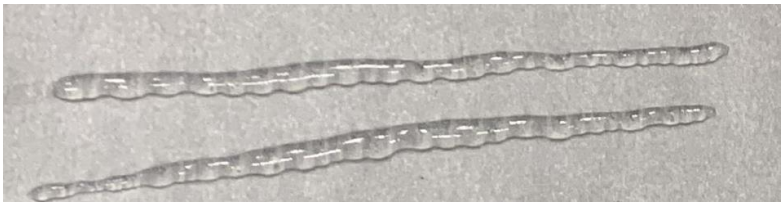

Figure 3

Manual extrusion of Aqueous Solution at 4% Weight Hydroxyethyl Cellulose

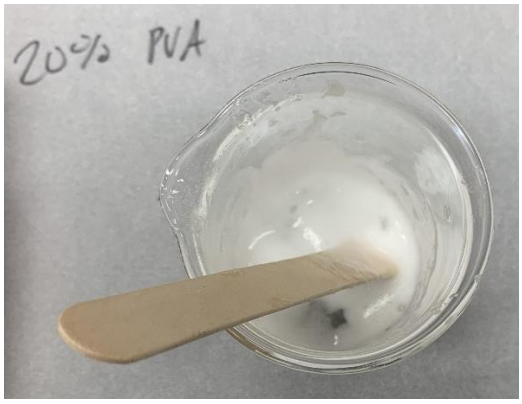

Figure 4

Significant Flocculation of Aqueous Solution at 20% Weight Polyvinyl Alcohol

Zinc powder was added to the binder solutions at 35-90%wt to visually determine a baseline. Zinc powder mixed with 4%wt HEC gel showed promising viscosity in the range of 70-80%wt. Zinc powder mixed with PVA solution did not show high enough viscosity for extrusion at any PVA concentration and was omitted from further experiments. It should be noted that zinc powder reduced the viscosity of pastes with both HEC and PVA binders. Additionally, solutions with a combination of HEC and PVA were not considered.

Figure 5

Manual Extrusion of the 15% PVA Aqueous Solution Mixed with 75% Zinc Powder, by Weight

Manual Printing

The HEC aqueous binder solution was originally held at 37ºC while mixing with magnetic stirrers until homogeneous, based on [67]. Increasing the temperature to 60ºC during mixing allowed the powder to dissolve and form a gel more readily. The zinc powder (75 wt%) was mixed for 20 minutes, using an overhead mixer, with an aqueous solution (3-4 wt%) of hydroxyethyl cellulose. Linear samples with L=7cm were manually extruded 5 layers high with a syringe and 0.1mm needle. Samples containing 3 wt% solution HEC did not show enough surface tension to hold their form. Samples containing 4 wt% HEC solution showed enough surface tension to withstand 5 layers of extrusion initially but started to run after approximately 5 minutes.

Figure 6

Manual Extrusion of the 4% HEC Aqueous Solution Mixed with 75% Zinc Powder, by Weight

This problem could potentially be resolved with convection drying, such as a fan or heater, during the printing process. Due to time constraints, casting was determined the most efficient method to form further samples with higher powder/binder ratios and heat treatment experimentation.

Heat Treatment

Using the mixing method mentioned above, zinc powder (80,90 wt%) was mixed with HEC solution (5,6,10 wt%) and cast into polystyrene dishes of 75x75x6 mm. Samples were allowed to dry at ambient temperature for at least 24 hours prior to heat treatment [68].

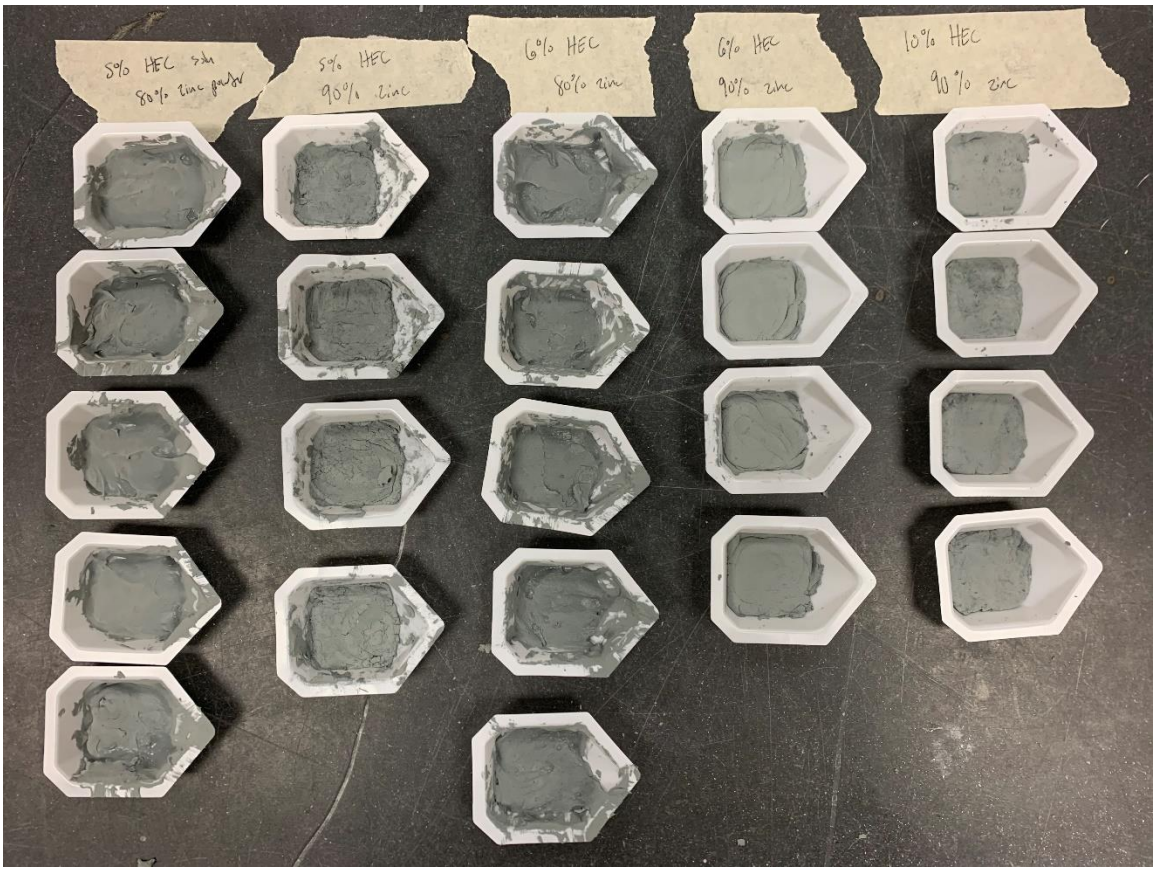

Figure 7

Dry Samples of HEC Solution Mixed with Zinc Powder at Various Ratios

The temperature range and sintering time for zinc powder has been studied in previous work [69]. Sintering refers to the process of heating powdered material to the point where a solid or porous mass forms without liquification of the material. Samples were sintered in a tube furnace under vacuum at a heating rate 5 ºC/min. Holding time was 2 hours, with temperatures ranging from 400-430 ºC to determine optimal sintering temperature. Completed samples were removed and stored in airtight storage containers to further cool and await testing.

Magnesium-Based Nanocomposites

Pure cast magnesium rods and $MgSm_2O_3$ (0.5%,1.0%,1.5%) nanocomposite rods were fabricated by Haghshenas et al. [41], using powder metallurgy accompanied by hybrid microwave sintering. Pure Mg powder (98.5% purity, Merck) and Sm_2O_3 nanoparticles (US Research Nanomaterials), with a particle size of 60-80nm, were blended with a RETSCH PM-400 mechanical alloying system. The alloys were cold compressed at 1-ksi uniaxial pressure into 35mm diameter and 40mm height "green" billets. Hybrid microwave sintering with a 2.45GHz, 900W Sharp microwave oven was then used cure the "green" billets at 630ºC [70]. The sintered samples were annealed for 2h at 450ºC and hot extruded in a 150-T hydraulic press at 400ºC with an extrusion ratio of 20.25:1 to produce rods of 8mm diameter [44].

After fabrication, samples were sectioned into small pieces for microstructure characterization. The fabricated nanocomposite samples were characterized for microstructure with a QUANTA FEG 650 Scanning Electron Microscope (SEM). Prior to the microstructure investigation, samples were polished via typical metallography procedure. The samples were then etched with a solution of 100mL ethanol, 2.5g picric acid, 25 mL acetic acid, and 25 mL distilled water.

Following microstructure characterization, the samples were cut into coupons approximately 3mm thick with a CNC lathe for electrochemical and immersion testing. Coupons were dry polished with 500-2000 grit sandpaper, at 100 grit increments, before EIS, PDP, and Immersion testing. Composition data for the modified simulated body fluid (m-SBF) is tabulated in Table 1.

Density

Two cylindrical samples of each nanocomposite composition were measured five times and a simple average was calculated. A hydrostatic densimeter, containing purified water, was used to collect density data. Theoretical and calculated density values were included for comparison. The equation for density calculation is shown below.

$$\rho = \frac{m}{V} \tag{9}$$

In Equation 9, m is the mass of the sample and V is the volume. The volume of a cylinder is given below as:

$$V = \pi \left(\frac{D}{2}\right)^2 \times h \tag{10}$$

where D is the diameter of the sample and h is the height. Porosity of measured samples was calculated using the following equation.

$$\%\ Porosity = \left(1 - \frac{\rho_{Measured,Avg}}{\rho_{Theoretical}}\right) \times 100 \tag{11}$$

In Equation 11, $\rho_{Measured,Avg}$ is the average measured density for a given sample and $\rho_{Theoretical}$ is the theoretical density of the sample. Theoretical density of a crystal structure is found using the equation:

$$\rho_{Theoretical} = \frac{Z \times M_W}{V_c \times N_A} \tag{12}$$

where Z is the number of atoms or molecules per unit cell, M_w is the molecular weight, V_c is the unit cell volume, and N_A is Avogadro's number.

Electrochemical Experiment Setup

A Gamry Interface 1010 Potentiostat was used for electrochemical testing. The 3-electrode experiment was used for Potentiodynamic Polarization and Electrochemical Impedance Spectroscopy corrosion tests. This is a standard testing procedure, which can be found on Gamry's company website [71]. The 3-electrode experiment consists of the working electrode, reference electrode, and counter electrode. The working electrode is the sample material to be used, which is connected to a copper wire and coated in insulative epoxy on all surfaces except the working surface. Figure 8 shows an example of one of the working electrodes. The reference electrode is shown in Figure 9a and consists of saturated calomel (Hg_2Cl_2). The counter electrode is a graphite cylinder and is shown in Figure 9b.

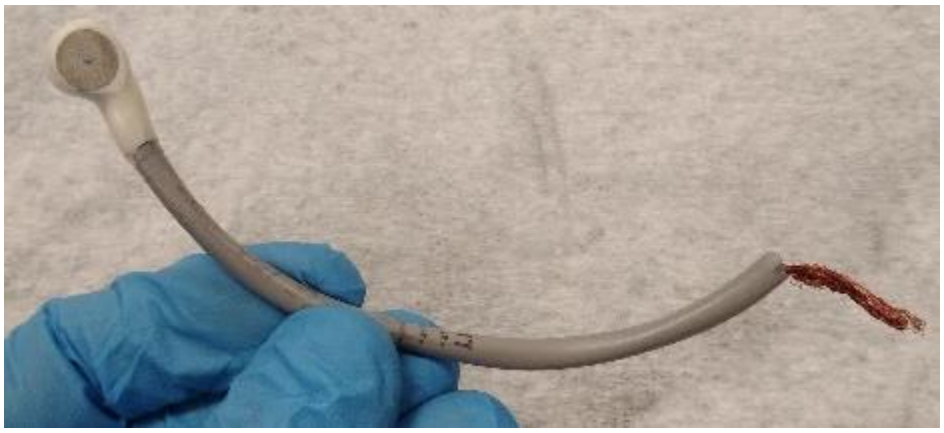

Figure 8

A Working Electrode used for Electrochemical Testing with Working Surface Displayed

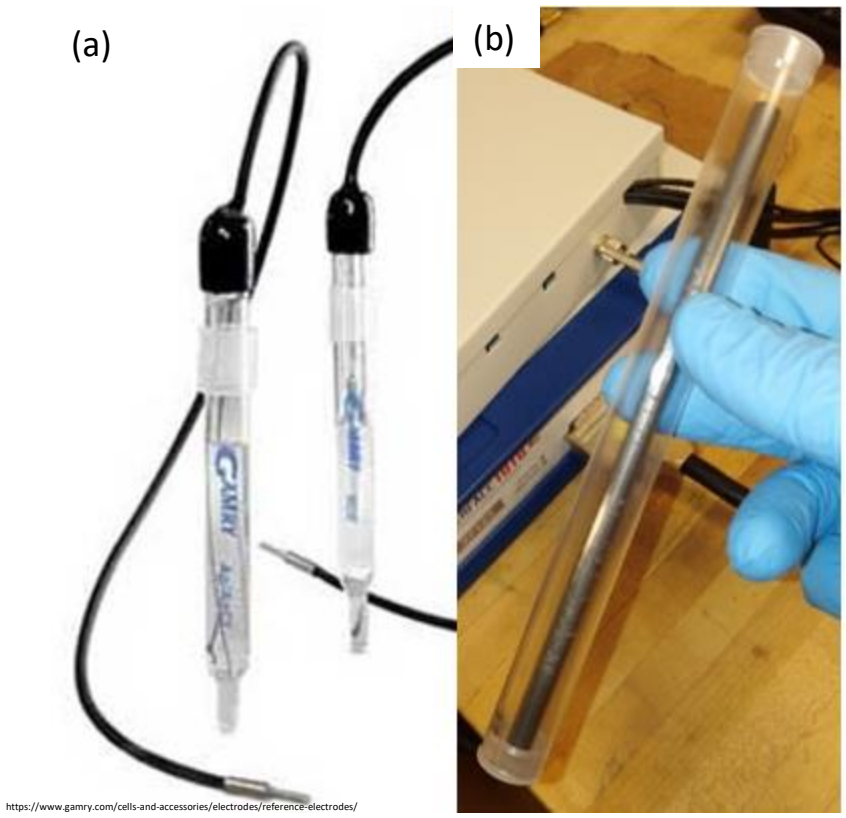

Figure 9

Pictures of the (a) Reference and (b) Counter Electrodes for Electrochemical Experiments

A wiring schematic for the 3-electrode experiment is shown in Figure 10. The Gamry interface includes 5 terminals, so two terminals were connected to both the working and counter electrode, per the instruction manual. Electrodes were submerged in simulated body fluid, from the same batch, for all experiments.

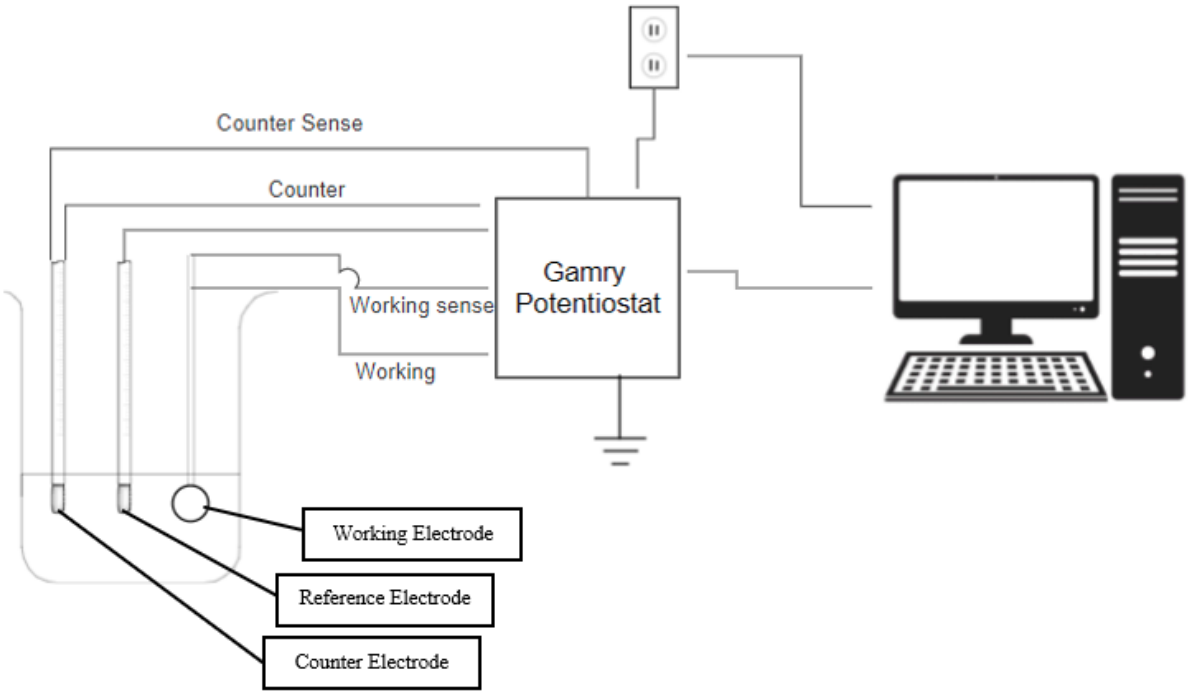

Figure 10

Wiring Diagram for 3-Electrode Experiment

PDP

Potentiodynamic Polarization testing was used to find the corrosion rate of each sample based on the Tafel anodic and cathodic slopes. Once the leads were connected, the Gamry Framework software was used for data acquisition. The “Tafel” DC corrosion experiment was used for these tests. Experimental parameters are shown in Figure 11.

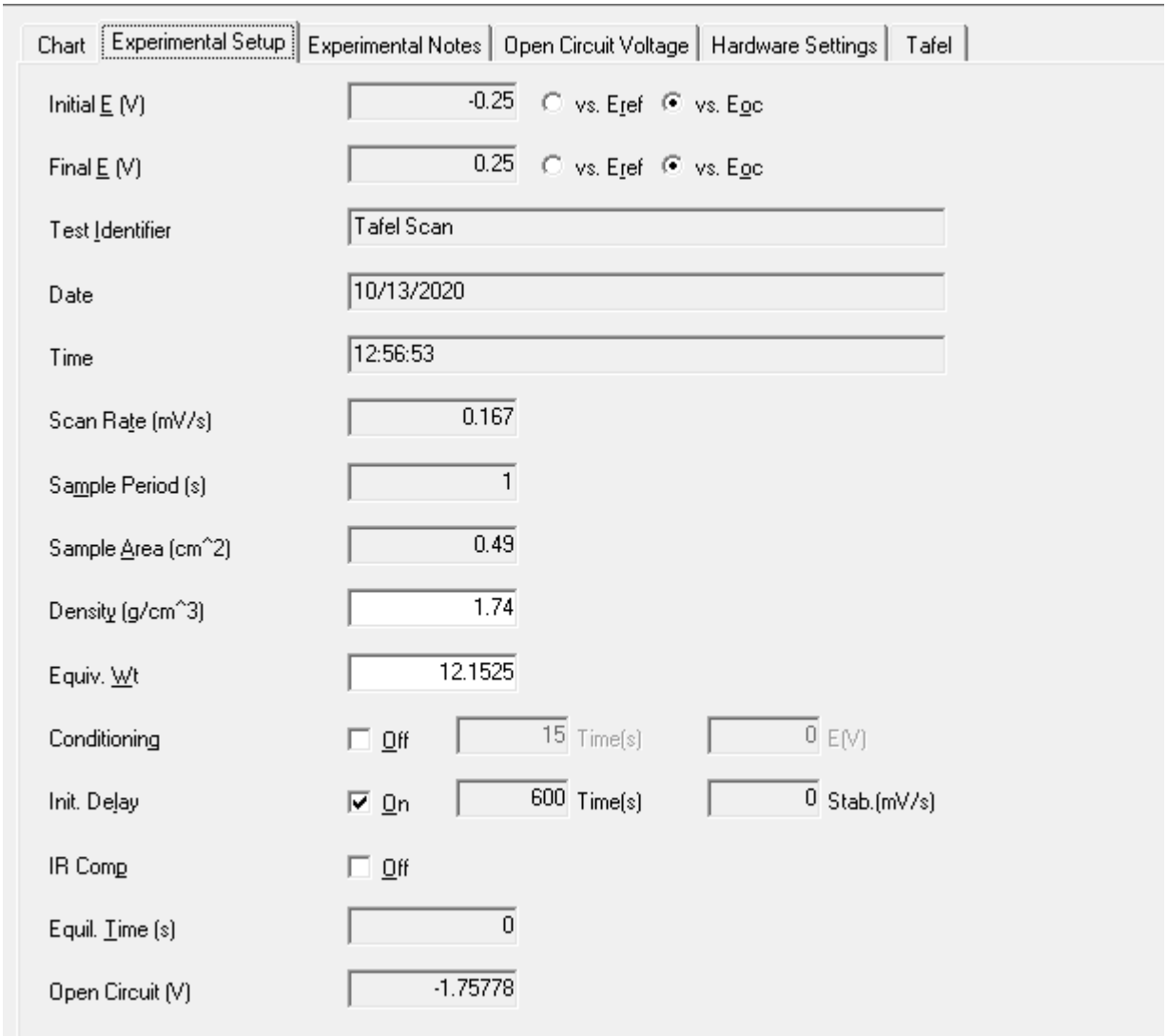

Figure 11

Parameters used for "Tafel" PDP testing of the Mg-Sm_2O_3 nanocomposites

The initial voltage "E" is where the cathodic scan starts. This should be set to a negative voltage, below the open circuit potential. The final voltage "E" determines how far above the open circuit potential the anodic scan will end. "Scan Rate" determines the voltage step size throughout the experiment. A lower value typically results in better data. However, higher scan rates are better for active metals because they react with solutions fast enough to cause a surface change during the experiment. The "Sample Period" represents the time between each data point. "Sample Area" is the surface area of the

sample exposed to the solution. The sample area for these experiments was a singular flat side of each cylinder. This can be seen on the working electrode in Figure 8. “Density” is the density of the material being tested. Measured density was used for this field. “Equiv. Wt” is the equivalent weight of the material (g), which is found using equation 13 [72].

$$EW = \sum \frac{f_i \times a_i}{n_i} \tag{13}$$

f_i is the mass fraction of each element i, a_i is the atomic weight of each element i, and n_i is the number of valence electrons of each element i. “Init. Delay” allows the sample to stabilize at open circuit potential before the test starts. The “Stab.” Option can be set to allow the test to begin before the initial delay time if the stability value is met. Once the parameters are set, the test can be started and will run until it reaches the final voltage.

The Gamry software includes a data analysis tool “Echem Analyst”, which was used to fit Tafel slopes to the data. The software has an automatic fitting tool, which was used by selecting a range of points. The most linear portion of each curve was chosen by observation. This is shown in Figure 12 using data from a sample of pure magnesium. Initial values are required to start the analysis. Figure 12 also shows default values from the above data, which were used for these experiments.

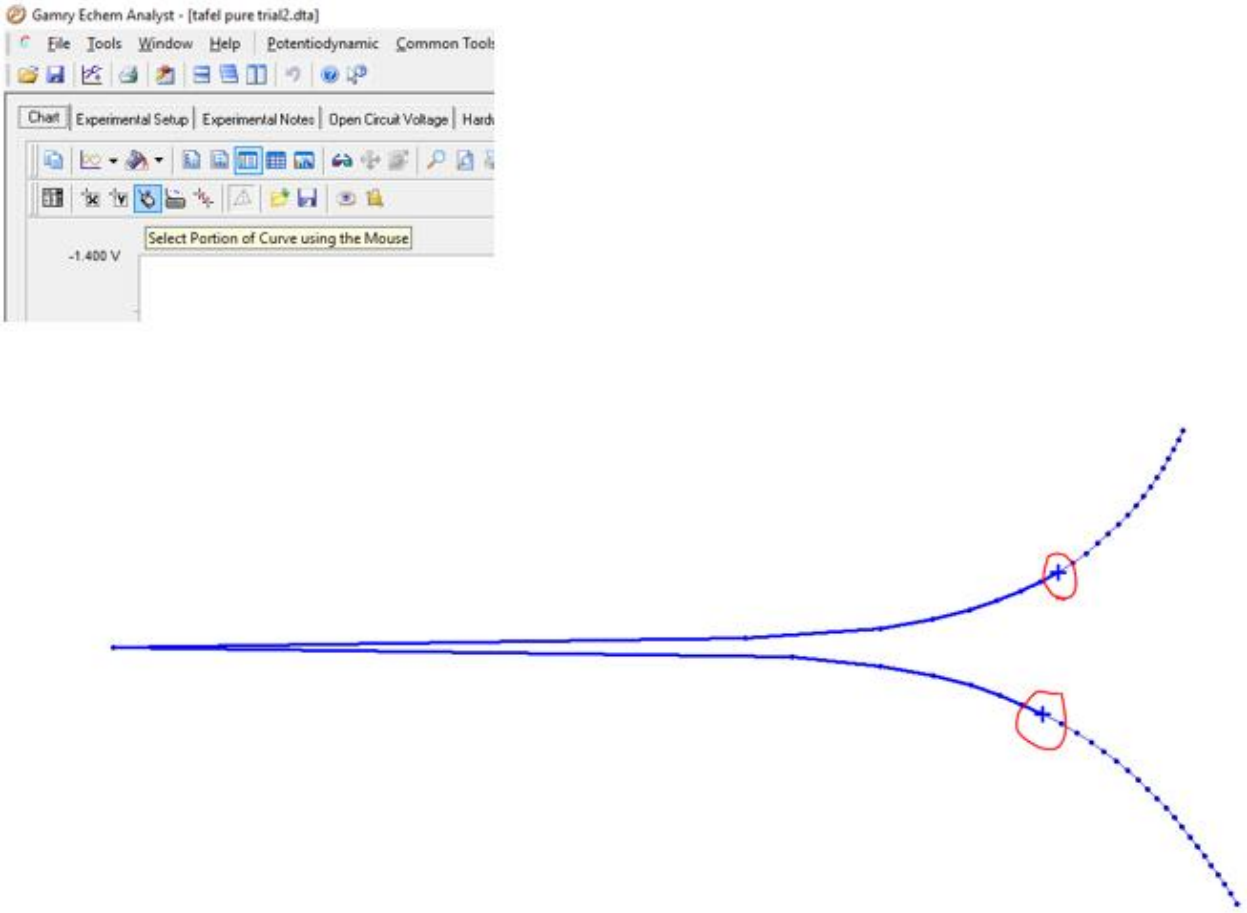

Figure 12

Selected Values for Tafel Curve Fitting

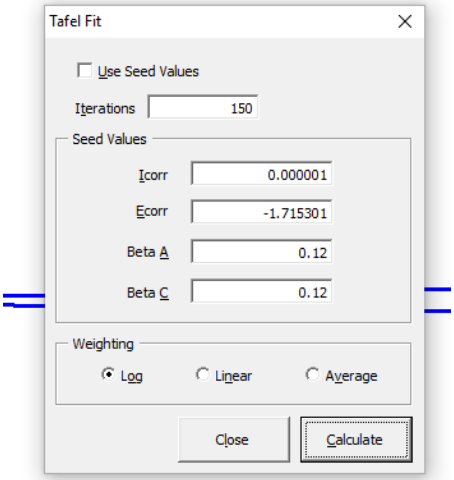

Figure 13

Menu for Initial Values of Data Analysis

Once the analysis is complete, the results are tabulated, and the corrosion rate is automatically calculated. This can be seen in Figure 14 below. Alternatively, the corrosion rate can be manually calculated, based on Faraday's Law, using equation 16. This is discussed further in the next section. This process was repeated for pure magnesium and each composition of magnesium nanocomposite.

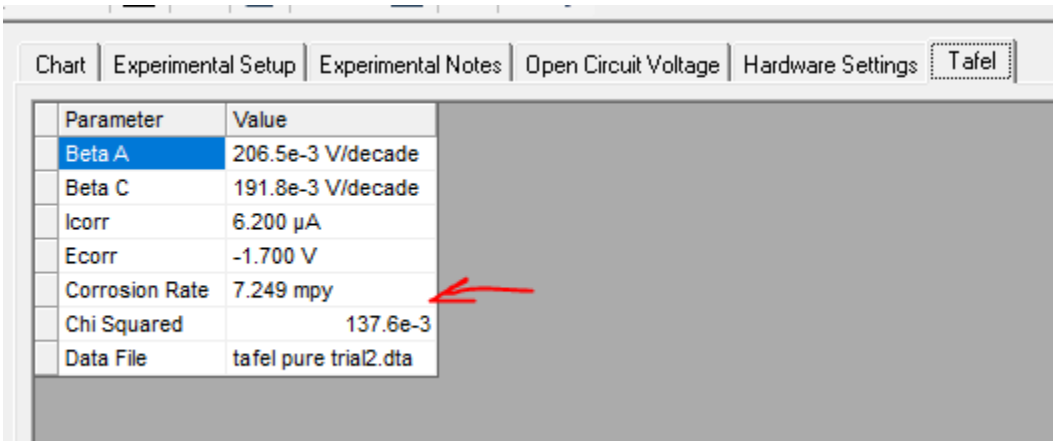

Figure 14

Results from a Tafel Experiment with Corrosion Rate Included

EIS

Electrochemical Impedance Spectroscopy (EIS) was used to find the polarization resistance of each sample for corrosion rate calculations. Once the electrodes were placed in the m-SBF solution with connected leads, Gamry Framework was used for data acquisition. The “Potentiostatic EIS” experiment was used for these tests. Experimental Parameters are shown in Figure 15.

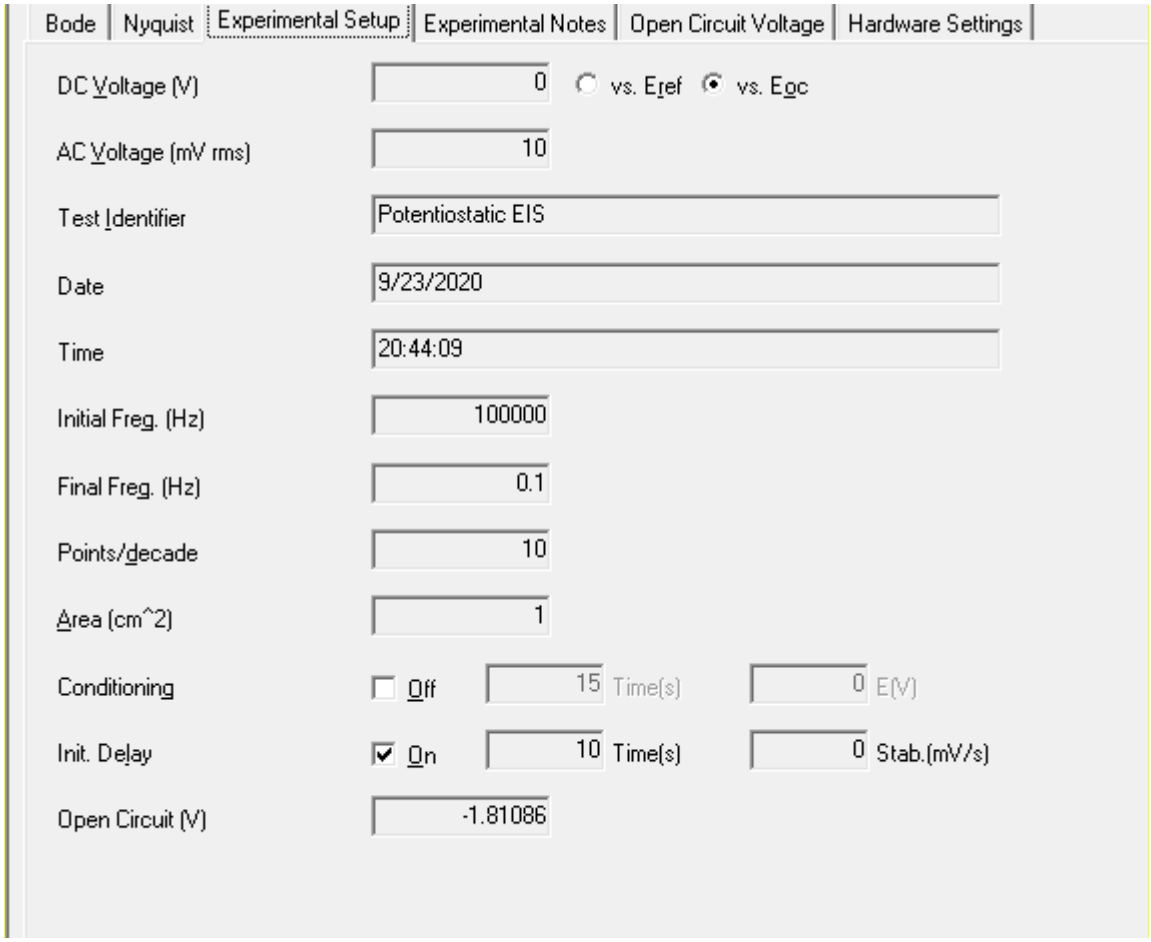

Figure 15

Parameters used for EIS Testing of the Mg-Sm_2O_3 Nanocomposites

A range of frequencies are scanned to differentiate cell component responses. The "Initial Freq." and "Final Freq." values are chosen accordingly. "Points/Decade" determines the amount of data points to be taken for each decade in frequency. The "AC Voltage" is the applied signal amplitude. A value of 10 mV or less is preferred to sustain linearity in the system. "Area" is the exposed surface area on the sample. This is the same area from PDP testing and seen in Figure 8. Once the parameters are set, the experiment can be started, and a Nyquist plot is developed. A sample Nyquist plot from Gamry Framework is shown in Figure 16 below. The first point of the plot represents the solution resistance R_s (R_u in Gamry software) and the diameter of the semicircle represents the polarization resistance R_p.

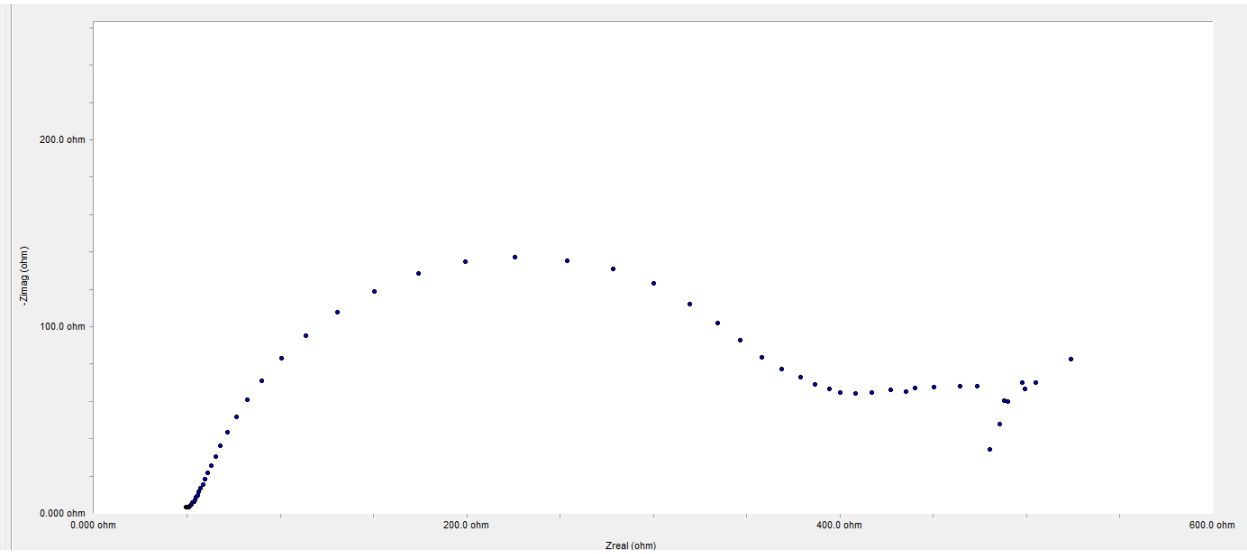

Figure 16

Generated Nyquist plot from an EIS Experiment

Once the plot is established for a given sample, an equivalent circuit is used to fit the data. The Gamry Echem Analyst includes a model editor for generating circuit models. A Randles circuit was used for curve fitting because of its semicircular shape. The Randles circuit for an uncoated magnesium alloy [73] is shown in Figure 17. This circuit includes solution resistance R_s, polarization resistance R_p, and charge transfer resistance of the electrochemical reaction R_t. The constant phase element (CPE) components Q_c and Q_{dl} represent the capacitance of the corrosion products layer and the capacitance of the double layer between the alloy and electrolyte solution, respectively.

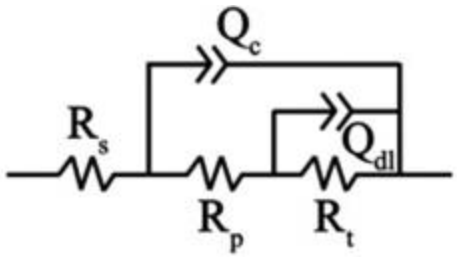

Figure 17

Randles Circuit used to Fit the Nyquist Plot Generated from EIS Experiments

Figure 18 shows the Nyquist plot fit with a CPE model including diffusion, from Gamry, and the discussed Randles circuit. A "Goodness of Fit" significance value is output for any given model. This can be seen in Figure 19. The level of confidence increases with a decreasing Goodness of Fit value. A value of 0.001183 provides strong evidence that the Nyquist curve is accurately fit with the modified Randles circuit.

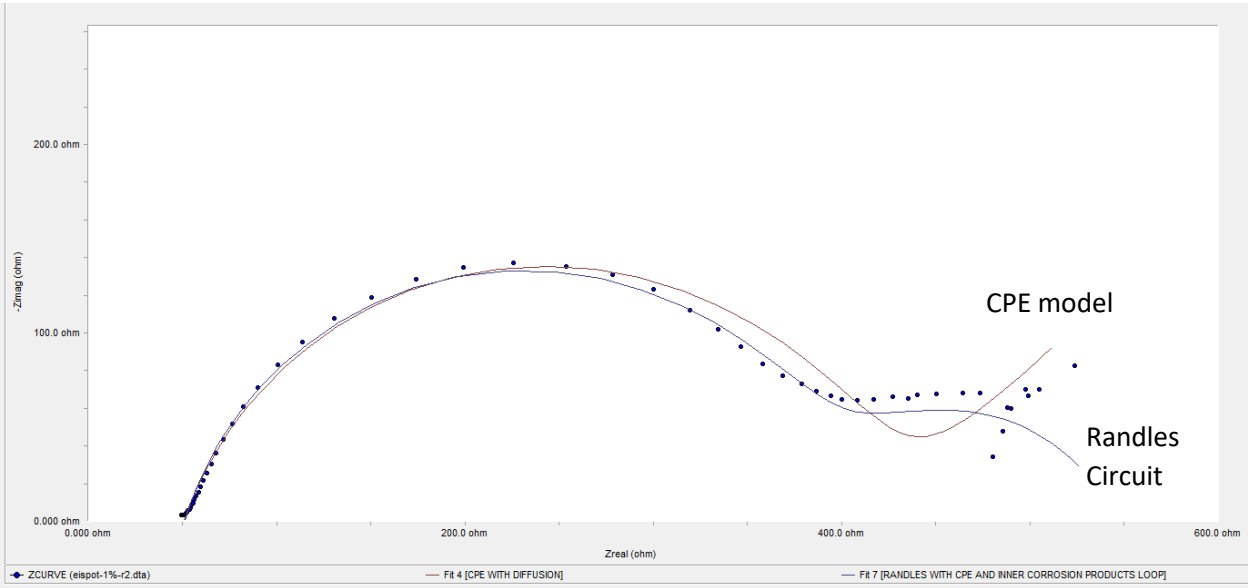

Figure 18

Nyquist Plot – Fit with CPE Model and Randles Circuit

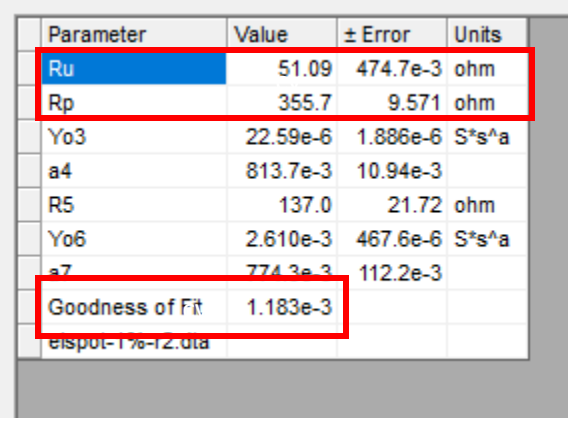

Parameter	Value	± Error	Units
Ru	51.09	474.7e-3	ohm
Rp	355.7	9.571	ohm
Yo3	22.59e-6	1.886e-6	S*s^a
a4	813.7e-3	10.94e-3	
R5	137.0	21.72	ohm
Yo6	2.610e-3	467.6e-6	S*s^a
a7	774.3e-3	112.2e-3	
Goodness of Fit	1.183e-3		
elspot-1%-12.dta			

Figure 19

Data Results from the Generated Nyquist Plot, Fit with Equivalent Randles Circuit

The corrosion rate is found, based on Faraday's Law, using the beta coefficients from Tafel slopes generated during PDP testing and corrosion current i_{corr} from polarization resistance of EIS testing. Equation 14 gives the proportionality constant of a system and requires the beta coefficients from Tafel slopes. Equation 15 relates the anodic and cathodic reactions from PDP testing to polarization resistance of EIS testing. Equation 15 is solved for the corrosion current. Equation 16 is based on Faraday's Law and is solved for the corrosion rate. Equivalent weight is calculated from Equation 13, found in the previous section.

$$B = \frac{b_a * b_c}{2.3\,(b_a + b_c)} \tag{14}$$

$$i_{corr} = \frac{B}{R_p} \tag{15}$$

$$CR = 3272\,\frac{EW * i_{corr}}{\rho * A} \tag{16}$$

For the equations above: B is the proportionality constant of a system in (V), b_a is the anodic reaction from Tafel data (Beta A), b_c is the cathodic reaction from Tafel data (Beta C), R_p is the polarization resistance (Ω) from EIS data (Ru), i_{corr} is the corrosion current (A), CR is the corrosion rate (mm/year), EW is the equivalent weight (g), ρ is the density of the material (g/cm^3), and A is the exposed surface area (cm^2).

Immersion

Immersion testing was performed using a modified simulated body fluid (m-SBF) at 37 ºC. Composition of the m-SBF is given in Table 1, with 500mL of ultra-pure water as the solvent. The solution was buffered with 1M HCl to a pH of 7.4. Samples of each composition (pure Mg, 0.5% $MgSm_2O_3$, 1.0% $MgSm_2O_3$, 1.5% $MgSm_2O_3$) were immersed in the m-SBF, then placed in an incubator for 5, 7, and 15 days. Figure 20 shows samples placed inside the incubation chamber. At each time point, the samples were removed from the solution, rinsed with de-ionized water, and weighed.

Table 1

Chemical Composition of the modified simulated body fluid (500 mL ultra-pure water as solvent)

Reagent	Amount (g)
NaCl	5.403
$NaHCO_3$ “sodium bicarbonate”	0.504
Na_2CO_3 “sodium carbonate”	0.426
KCl “potassium chloride”	0.225
$K_2HPO_43H_2O$ “Potassium Phosphate, Dibasic Trihydrate”	0.23
$MgCl_26H_2O$ “Magnesium chloride, Hexahydrate”	0.311
HEPES	17.892 in 100 ml of 0.2M NaOH
$CaCl_2$	0.293
Na_2SO_4	0.072
1M NaOH (mL)	15

Figure 20

Magnesium Nanocomposite Samples, Ready for Incubation

The corrosion rates of the samples were calculated based on mass loss using the following equation [32]:

$$CR = \frac{tW}{ATρ} \times 10 \quad (17)$$

where CR is the corrosion rate (mm/year), t is 365 × 24(h), W is the mass loss (g), A is the original surface area exposed to the corrosive media (cm^2), T is the immersion time (h), and ρ is the sample standard density (g/cm^3). Two samples of each composition were tested for an average result.

CHAPTER IV

RESULTS & DISCUSSION

Density

Table 2 shows the averaged density measurements for pure Mg and fabricated nanocomposites. Raw data for density measurements and calculations can be found in Appendix A. It can be seen from Table 2 that the average measured values are more consistent with theoretical values than the average calculated values. This is possibly due to lack of caliper resolution when measuring the diameters and heights of samples for calculated values. Porosity values <5% suggest sample fabrication was of high quality and should provide lower corrosion rates.

Table 2

Average Density Measurements and Calculated Density for Pure Mg and $MgSm_2O_3$ Nanocomposites

Composition	Calculated Avg (g/cm^3)	Measured Avg (g/cm^3)	Standard Deviation (g/cm^3)	Theoretical Density (g/cm^3)	% Porosity
Pure	1.607862	1.7255	± 0.081401	1.73800	0.719217
0.5%	1.662268	1.7160	± 0.044370	1.77106	3.108873
1%	1.663629	1.7749	± 0.091510	1.81281	2.091229
1.5%	1.752242	1.7901	± 0.12115	1.85456	3.475757

Microstructure

SEM micrographs of 1% concentration $MgSm_2O_3$ are shown in Figure 21. Deformed grain boundaries can be seen in Figure 21c and Figure 21d. It is likely that a high extrusion ratio (20.25:1) is the cause of this grain boundary deformation. However, a higher extrusion ratio promotes the homogeneous dispersion of nanoparticles into the matrix [41]. These Sm_2O_3 nanoparticles can be faintly observed in Figure 21a and Figure 21b. A higher magnification should reveal that the nanoparticles are pinned to the recrystallized grain boundaries, based on a similar microstructure study by Haghshenas et al. [41]. The majority of grain sizes are between 30-50 microns, which is observed in Figure 22. Microstructure data gathered from varied volume fractions of Sm_2O_3 may reveal a connection between grain refinement and nanocomposite concentration.

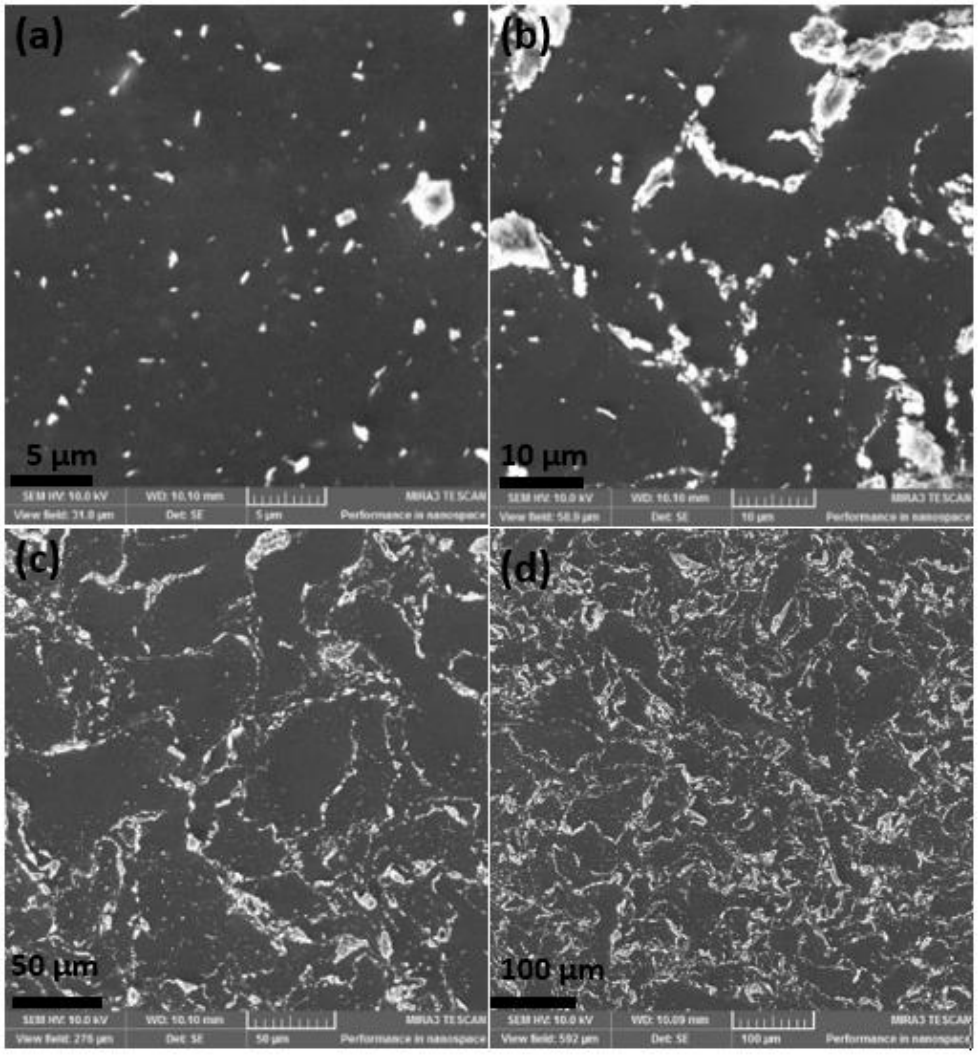

Figure 21

SEM micrographs of fabricated $MgSm_2O_3$ at 1% concentration with view fields of (a) 31µm, (b) 58.9 µm, (c) 276 µm, and (d) 592 µm

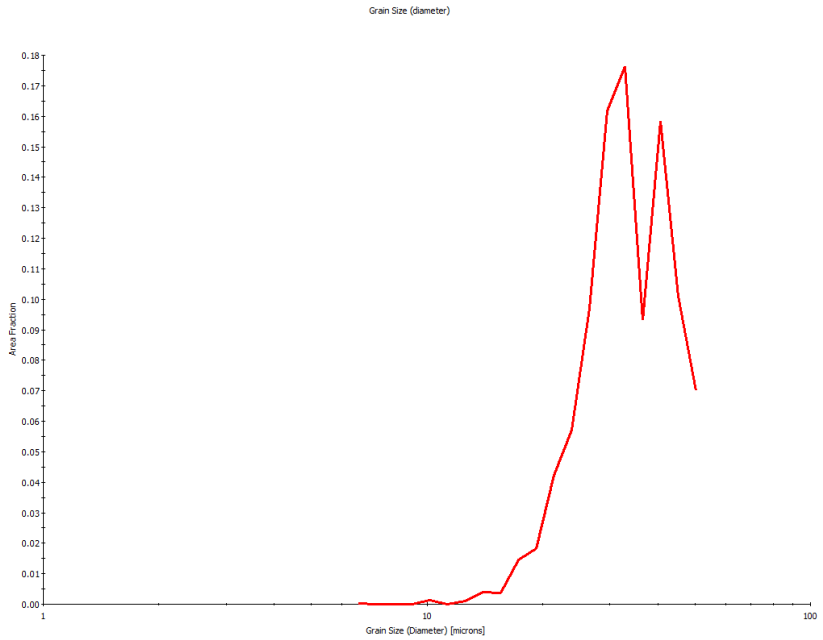

Figure 22

Grain Size Distribution Curve of Fabricated $MgSm_2O_3$ at 1% Concentration

Potentiodynamic Polarization

Corrosion rates found through potentiodynamic polarization are shown in Figure 23. All three nanocomposites resulted in lower corrosion rates than pure magnesium. The corrosion rate of $MgSm_2O_3$ nanocomposites decreases when the concentration of Sm_2O_3 nanoparticles increases from 0.5% to 1%. However, as the concentration moves above 1%, the corrosion rate begins to increase again. Table 3 lists the results of Tafel DC corrosion experiments. It can be seen that the anodic Tafel slopes (β_A) of all samples are larger than the cathodic Tafel slopes (β_C), which suggests that the corrosion processes were controlled by the anode reactions. The relationship between Tafel slopes, polarization resistance, and corrosion rate is seen in equations 14-16. It is likely that the relatively smaller proportionality constant (B) of 1.5% Sm_2O_3, affected by the anodic and cathodic Tafel slopes, is the culprit for its higher corrosion rate. The corrosion current densities (I_{corr}) of the 1% and 1.5% nanocomposites are significantly higher than those of pure Mg and the 0.5% Sm_2O_3 nanocomposite. This would suggest that the 1%

nanocomposite should have a higher corrosion rate as well, but its relatively high proportionality constant value outweighs its corrosion current density. Based on results from PDP experimentation, Mg-Sm_2O_3 nanocomposites show improved corrosion rates up to 1% Sm_2O_3 and an increase in the corrosion rate as concentration of Sm_2O_3 exceeds 1%.

Table 3

Data collected from Potentiodynamic Polarization experiments with calculated proportionality constants

Potentiodynamic Polarization				
Composition	Pure Cast Mg	0.5% Sm_2O_3	1% Sm_2O_3	1.5% Sm_2O_3
β_A (V/decade)	0.1395	0.3932	0.6937	1.092
β_C (V/decade)	0.1294	0.368	0.3944	0.1236
B (V)	0.0292	0.0826	0.1093	0.0483
I_{corr} (µA)	142	365	1260	1040
E_{corr} (V)	-1.78	-1.73	-1.97	-1.92
Corr Rate (mm/yr)	19.14	15.93	11.13	13.64

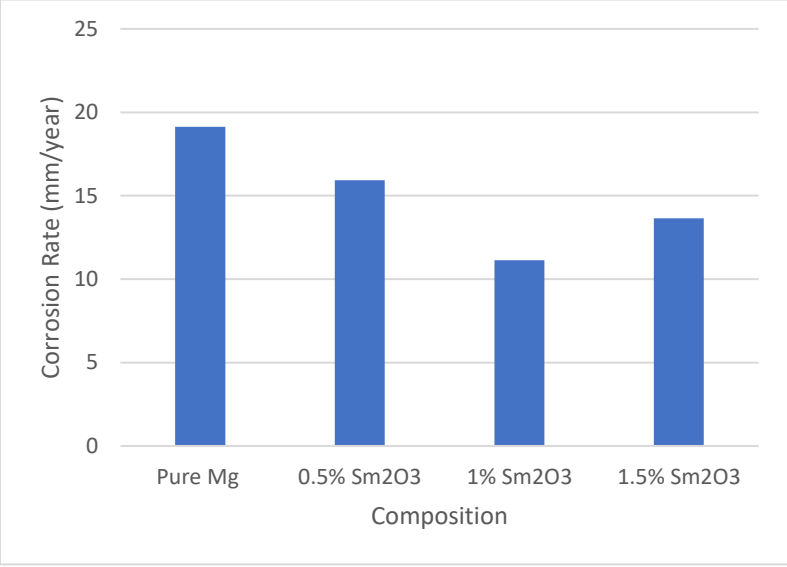

Figure 23

Corrosion Rates from PDP Testing of Pure Mg and Mg-Sm_2O_3 Nanocomposites

Electrochemical Impedance Spectroscopy

Corrosion rates found via electrochemical impedance spectroscopy are shown in Figure 24. It can be seen that the Mg-1%Sm_2O_3 nanocomposite was the only composition to result in a lower corrosion rate than pure magnesium. However, the nanocomposites' corrosion rates follow the same trend as rates found via PDP testing. The main difference lies with the 1.5% Sm_2O_3 nanocomposite. EIS testing resulted in a significantly higher corrosion rate as the Sm_2O_3 concentration exceeded 1%. Higher corrosion rates of the nanocomposites are likely the result of initial degradation during the test, since EIS is more sensitive to instantaneous changes during the test. This suggests that the initial degradation of Mg-Sm_2O_3 nanocomposites is faster than that of pure magnesium. Data collected from EIS testing with calculated corrosion currents and corrosion rates are listed in Table 4. Polarization resistance (R_p) of the Mg-1%Sm_2O_3 nanocomposite is significantly higher than the other nanocomposites, which agrees with its lower corrosion rate. Intuitively, the higher polarization resistance would seem to result in a much lower corrosion rate of the 1% nanocomposite. Similarly, the low polarization resistance of pure magnesium would suggest that its corrosion rate would be much higher. This can be attributed to their relative proportionality constant (B) values, calculated from the Tafel slopes. Results from EIS testing agree with PDP testing results, where Mg-Sm_2O_3 nanocomposites show optimal corrosion rates up to 1% Sm_2O_3 and an increasing corrosion rate as the concentration of Sm_2O_3 exceeds 1%.

Table 4

Data collected from Electrochemical Impedance Spectroscopy experiments with calculated corrosion currents and corrosion rates

Electrochemical Impedance Spectroscopy				
Composition	Pure Cast Mg	0.5% Sm_2O_3	1% Sm_2O_3	1.5% Sm_2O_3
Rp (Ω)	71.015	241.66	457.42	164.76
Ru (Ω)	34.2	52.72	49.23	47.62
Cf (F)	1.34E-05	1.05E-05	8.14E-06	7.18E-06
Fit	1.90E-02	2.50E-02	1.33E-02	1.72E-02
i_{corr} (A)	0.000411	0.000342	0.000239	0.000293
CR (mm/yr)	24.26	26.29	22.31	36.54

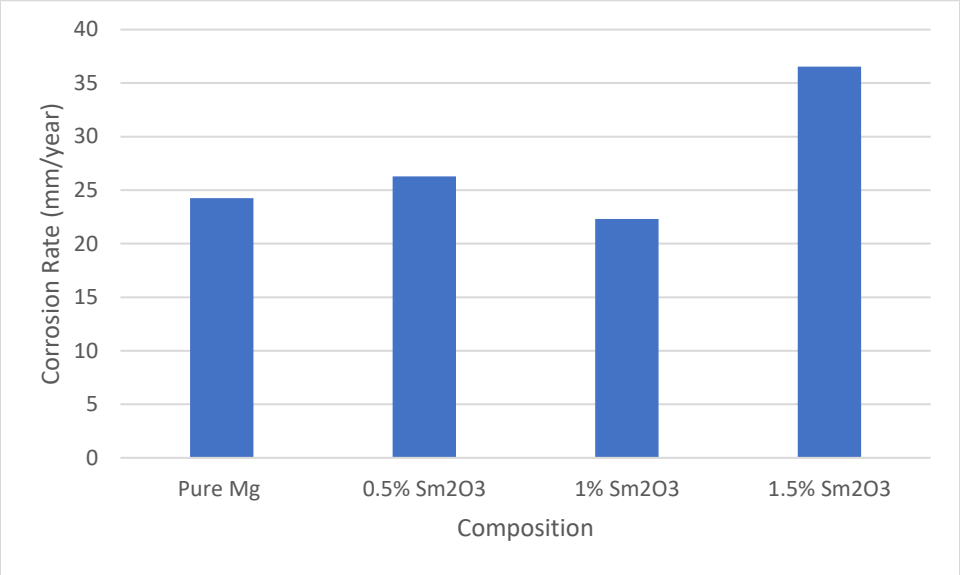

Figure 24

Corrosion Rates from EIS Testing of Pure Mg and Mg-Sm_2O_3 Nanocomposites

Immersion Testing

Figure 25 displays the corrosion rates calculated based on weight loss during immersion testing. It is clear that the corrosion rates of the magnesium nanocomposites follow the same trend as rates from electrochemical testing. Additionally, all corrosion rates calculated from immersion testing are close to the rates found during PDP testing. Pure magnesium shows the most significant drop of corrosion rate after 7 days of immersion. The decrease in corrosion rate is likely a representation of the protective magnesium hydroxide layer formation after initial degradation. The initial degradation after 5 days is visible in Figure 26a, 26d, 26g, and 26j. This delayed decrease in corrosion rate can also be observed in the magnesium nanocomposites to a lesser extent. The degradation of pure magnesium, Mg-0.5%Sm_2O_3, and Mg-1.5%Sm_2O_3, with the presence of large cracked regions on the surface of the samples, is apparent after 7 days in Figure 26b, 26e, and 26k, respectively. Further degradation of Mg-0.5%Sm_2O_3 and Mg-1.5%Sm_2O_3 can be observed in Figure 26f, and 26i, while pure magnesium started to corrode in a more uniform manner after 15 days in Figure 26c. On the other hand, the Mg-1%Sm_2O_3 nanocomposite showed a uniform shape without a significant degradation at any point during the immersion testing. This can be observed in Figure 26g-i. Corrosion rates determined via immersion testing agree with corrosion rates found through electrochemical testing. The Mg-1%Sm_2O_3 nanocomposite shows optimal corrosion rates when calculated via electrochemical and immersion testing.

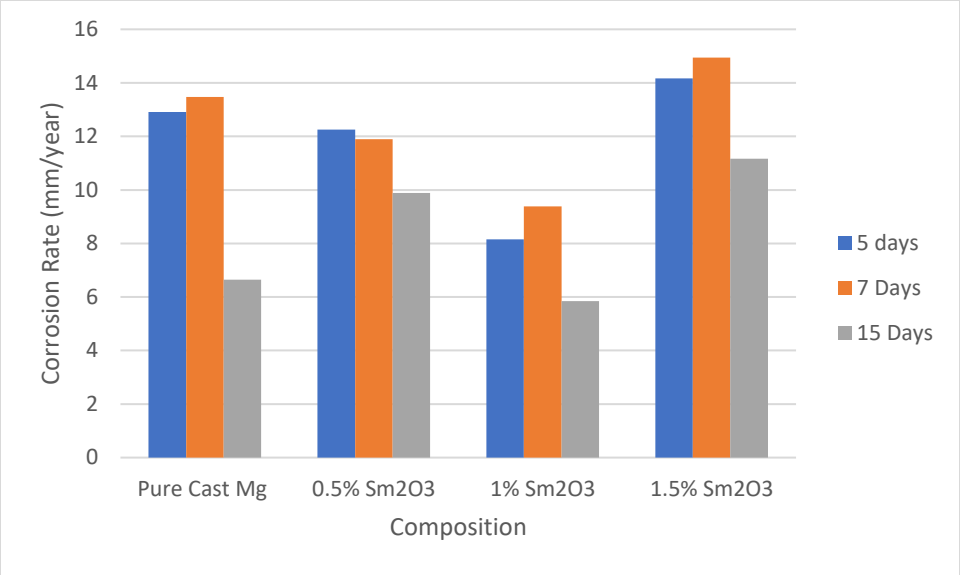

Figure 25

Immersion Test Data Comparing Pure Mg and $MgSm_2O_3$ Nanocomposites Ranging from 0.5-1.5%

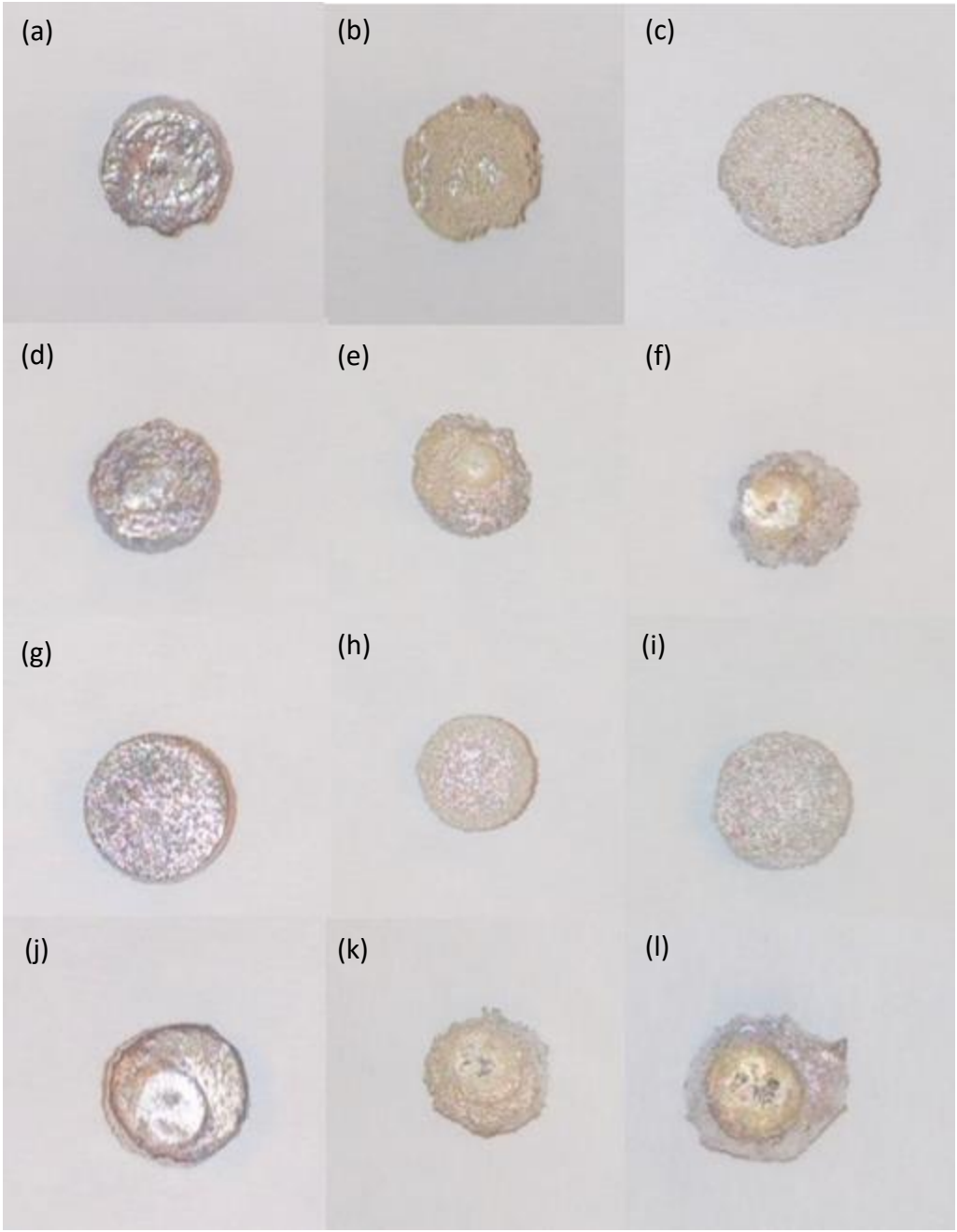

Figure 26

Images of samples after immersion testing: Pure Magnesium after (a) 5 days, (b) 7 days, and (c) 15 days, Mg-0.5%Sm_2O_3 after (d) 5 days, (e) 7 days, and (f) 15 days, Mg-1%Sm_2O_3 after (g) 5 days, (h) 7 days, and (i) 15 days, and Mg-1.5%Sm_2O_3 after (j) 5 days, (k) 7 days, and (l) 15 days.

CHAPTER V

CONCLUSIONS

In vitro degradation of pure magnesium and fabricated Mg-Sm_2O_3 nanocomposites was explored through Potentiodynamic Polarization, Electrochemical Impedance Spectroscopy, and Immersion testing. The addition of the Sm_2O_3 nanoparticles to the Mg matrix resulted in enhancement in the corrosion resistance in addition to its well-established positive effect on the mechanical properties. The 1% volume fraction of Sm_2O_3 was found to be the optimal content for a reduced corrosion rate (PDP: 11.13 mm/yr, EIS: 22.31 mm/yr, Immersion: 5.84 mm/yr at day 15) compared to pure magnesium (PDP: 19.14 mm/yr, EIS: 24.26 mm/yr, Immersion: 6.64 mm/yr at day 15). The corrosion rate of Mg-Sm_2O_3 nanocomposites increased when the volume fraction of Sm_2O_3 exceeded 1%. Mg-1%Sm_2O_3 consistently showed a corrosion rate lower than pure magnesium through all three corrosion testing methods. Uniform corrosion of Mg-1%Sm_2O_3 was visually observed from immersion testing photographs. Further experimentation with corrosion and mechanical testing of the nanocomposites may validate 1% volume Sm_2O_3 as the optimal content for orthopedic applications.

A viscous zinc paste was explored as a medium for additive manufacturing biodegradable metals at a low temperature. Manual extrusion was successful up to 5 layers with a paste containing 4% HEC aqueous solution and zinc powder at a ratio of 1:3, respectively. Restraints on time and resources prevented further extrusion testing and initial testing of the heat-treated samples. Future work will include utilization of atomized, spherical powder and extrusion printers. This experimentation broadens the possibilities for patient-specific medical devices. Efficient medical treatment is an open-ended process which requires constant experimentation. As medical technology advances, the development of biodegradable materials provides a path to a new standard of patient care.

REFERENCES

1. Wu, S., et al., *Surface nano-architectures and their effects on the mechanical properties and corrosion behavior of Ti-based orthopedic implants.* Surface and Coatings Technology, 2013. **233**: p. 13-26.

2. Sheikh, Z., et al., *Biodegradable Materials for Bone Repair and Tissue Engineering Applications.* Materials, 2015. **8**(9): p. 5744-5794.

3. Han, H.-S., et al., *Current status and outlook on the clinical translation of biodegradable metals.* Materials Today, 2019. **23**: p. 57-71.

4. Zhang, S., et al., *Research on an Mg-Zn alloy as a degradable biomaterial.* Acta biomaterialia, 2009. **6**: p. 626-40.

5. Seal, C.K., K. Vince, and M.A. Hodgson, *Biodegradable surgical implants based on magnesium alloys – A review of current research.* IOP Conference Series: Materials Science and Engineering, 2009. **4**: p. 012011.

6. Joseph, B., et al., *Polymer sutures for simultaneous wound healing and drug delivery – A review.* International Journal of Pharmaceutics, 2017. **524**(1): p. 454-466.

7. Witte, F., et al., *In vivo corrosion of four magnesium alloys and the associated bone response.* Biomaterials, 2005. **26**(17): p. 3557-3563.

8. Hartwig, A., *Role of magnesium in genomic stability.* Mutation Research/Fundamental and Molecular Mechanisms of Mutagenesis, 2001. **475**(1): p. 113-121.

9. Vormann, J., *Magnesium: nutrition and metabolism.* Molecular aspects of medicine, 2003. **24**(1-3): p. 27-37.

10. Okuma, T., *Magnesium and bone strength.* Nutrition, 2001. **17**(7): p. 679-680.

11. *Magnesium in Human Health and Disease*. 1st ed. 2013. ed. Nutrition and Health, ed. R.R. Watson, V.R. Preedy, and S. Zibadi. 2013, Totowa, NJ: Humana Press.

12. Frankel, G.S., A. Samaniego, and N. Birbilis, *Evolution of hydrogen at dissolving magnesium surfaces.* Corrosion Science, 2013. **70**: p. 104-111.

13. Noviana, D., et al., *The effect of hydrogen gas evolution of magnesium implant on the postimplantation mortality of rats.* Journal of Orthopaedic Translation, 2016. **5**: p. 9-15.

14. Zhao, D., et al., *Vascularized bone grafting fixed by biodegradable magnesium screw for treating osteonecrosis of the femoral head.* Biomaterials, 2016. **81**: p. 84-92.

15. Han, H.-S., et al., *Current status and outlook on the clinical translation of biodegradable metals.* Materials today (Kidlington, England), 2019. **23**: p. 57-71.

16. Witte, F., et al., *Degradable biomaterials based on magnesium corrosion.* Current Opinion in Solid State and Materials Science, 2008. **12**(5): p. 63-72.

17. Aghion, E., G. Levy, and S. Ovadia, *In vivo behavior of biodegradable Mg–Nd–Y–Zr–Ca alloy.* Journal of Materials Science: Materials in Medicine, 2012. **23**(3): p. 805-812.

18. Zeng, R.-C., et al., *Corrosion and characterisation of dual phase Mg–Li–Ca alloy in Hank's solution: The influence of microstructural features.* Corrosion Science, 2014. **79**: p. 69-82.

19. Höhn, S., S. Virtanen, and A.R. Boccaccini, *Protein adsorption on magnesium and its alloys: A review.* Applied Surface Science, 2019. **464**: p. 212-219.

20. Zainal Abidin, N.I., et al., *Corrosion of high purity Mg, Mg2Zn0.2Mn, ZE41 and AZ91 in Hank's solution at 37°C.* Corrosion Science, 2011. **53**(11): p. 3542-3556.

21. Ghoneim, A.A., A.M. Fekry, and M.A. Ameer, *Electrochemical behavior of magnesium alloys as biodegradable materials in Hank's solution.* Electrochimica Acta, 2010. **55**(20): p. 6028-6035.

22. He, W., E. Zhang, and K. Yang, *Effect of Y on the bio-corrosion behavior of extruded Mg–Zn–Mn alloy in Hank's solution.* Materials Science and Engineering: C, 2010. **30**(1): p. 167-174.

23. Kirkland, N.T., N. Birbilis, and M.P. Staiger, *Assessing the corrosion of biodegradable magnesium implants: A critical review of current methodologies and their limitations.* Acta Biomaterialia, 2012. **8**(3): p. 925-936.

24. Walker, J., et al., *Magnesium alloys: Predicting in vivo corrosion with in vitro immersion testing.* Journal of biomedical materials research. Part B, Applied biomaterials, 2012. **100B**(4): p. 1134-1141.

25. Zhang, E., et al., *In vivo evaluation of biodegradable magnesium alloy bone implant in the first 6 months implantation.* Journal of Biomedical Materials Research Part A, 2009. **90A**(3): p. 882-893.

26. Dziuba, D., et al., *Long-term in vivo degradation behaviour and biocompatibility of the magnesium alloy ZEK100 for use as a biodegradable bone implant.* Acta Biomaterialia, 2013. **9**(10): p. 8548-8560.

27. Liu, C., et al., *Biodegradable Magnesium Alloys Developed as Bone Repair Materials: A Review.* Scanning, 2018. **2018**: p. 15.

28. Sanchez, A.H.M., et al., *Mg and Mg alloys: How comparable are in vitro and in vivo corrosion rates? A review.* Acta Biomaterialia, 2015. **13**: p. 16-31.

29. Xue, D., et al., *In Vivo and In Vitro Degradation Behavior of Magnesium Alloys as Biomaterials.* Journal of Materials Science & Technology, 2012. **28**(3): p. 261-267.

30. Witte, F., et al., *In vitro and in vivo corrosion measurements of magnesium alloys.* Biomaterials, 2006. **27**(7): p. 1013-1018.

31. Hofstetter, J., et al., *Assessing the degradation performance of ultrahigh-purity magnesium in vitro and in vivo.* Corrosion Science, 2015. **91**: p. 29-36.

32. Wen, Z., et al., *Corrosion behaviors of Mg and its alloys with different Al contents in a modified simulated body fluid.* Journal of Alloys and Compounds, 2009. **488**(1): p. 392-399.

33. Angrisani, N., et al., *Biocompatibility and degradation of LAE442-based magnesium alloys after implantation of up to 3.5years in a rabbit model.* Acta Biomaterialia, 2016. **44**: p. 355-365.

34. *Biodegradable Metals*. 2018: MDPI - Multidisciplinary Digital Publishing Institute.

35. Liu, J., et al., *Comparative in vitro study on binary Mg-RE (Sc, Y, La, Ce, Pr, Nd, Sm, Eu, Gd, Tb, Dy, Ho, Er, Tm, Yb and Lu) alloy systems.* Acta biomaterialia, 2020. **102**: p. 508-528.

36. Hort, N., et al., *Magnesium alloys as implant materials – Principles of property design for Mg–RE alloys.* Acta Biomaterialia, 2010. **6**(5): p. 1714-1725.

37. *Surface modification of magnesium and its alloys for biomedical applications. Volume 2 : modification and coating techniques*. Woodhead Publishing Series in Biomaterials ; Number 90, ed. T.S.N.S. Narayanan, I.-S. Park, and M.H. Lee. 2015, Cambridge, England: Woodhead Publishing.

38. Li, L.-Y., et al., *Advances in functionalized polymer coatings on biodegradable magnesium alloys – A review.* Acta Biomaterialia, 2018. **79**: p. 23-36.

39. Yin, Z.-Z., et al., *Advances in coatings on biodegradable magnesium alloys.* Journal of Magnesium and Alloys, 2020. **8**(1): p. 42-65.

40. Haghshenas, M. and M. Gupta, *Magnesium nanocomposites reinforced with rare earth element nanoparticles: nanoindentation-driven response.* Nanocomposites, 2020. **6**(1): p. 22-30.

41. Haghshenas, M., et al., *Magnesium–samarium oxide nanocomposites: Room-temperature depth-sensing nanoindentation response.* International Journal of Lightweight Materials and Manufacture, 2020. **3**(3): p. 217-225.

42. Robson, J.D., et al., *Grain Boundary Segregation of Rare-Earth Elements in Magnesium Alloys.* Metallurgical and materials transactions. A, Physical metallurgy and materials science, 2016. **47**(1): p. 522-530.

43. Hassan, S.F. and M. Gupta, *Development of nano-Y2O3 containing magnesium nanocomposites using solidification processing.* Journal of alloys and compounds, 2007. **429**(1-2): p. 176-183.

44. Kujur, M.S., et al., *Significantly Enhancing the Ignition/Compression/Damping Response of Monolithic Magnesium by Addition of Sm2O3 Nanoparticles.* Metals (Basel), 2017. **7**(9): p. 357.

45. Parai, R. and S. Bandyopadhyay-Ghosh, *Engineered bio-nanocomposite magnesium scaffold for bone tissue regeneration.* Journal of the mechanical behavior of biomedical materials, 2019. **96**: p. 45-52.

46. Razavi, M., M.H. Fathi, and M. Meratian, *Fabrication and characterization of magnesium–fluorapatite nanocomposite for biomedical applications.* Materials Characterization, 2010. **61**(12): p. 1363-1370.

47. Tapiero, H. and K.D. Tew, *Trace elements in human physiology and pathology: zinc and metallothioneins.* Biomedicine & Pharmacotherapy, 2003. **57**(9): p. 399-411.

48. Berg, J.M. and Y. Shi, *The galvanization of biology: A growing appreciation for the roles of zinc.* Science, 1996. **271**(5252): p. 1081.

49. Plum, L.M., L. Rink, and H. Haase, *The essential toxin: impact of zinc on human health.* International journal of environmental research and public health, 2010. **7**(4): p. 1342-1365.

50. King, J.C., D.M. Shames, and L.R. Woodhouse, *Zinc homeostasis in humans.* The Journal of nutrition, 2000. **130**(5): p. 1360S-1366S.

51. Moonga, B.S. and D.W. Dempster, *Zinc is a potent inhibitor of osteoclastic bone resorption in vitro.* Journal of Bone and Mineral Research, 1995. **10**(3): p. 453-457.

52. Li, H.F., et al., *Development of biodegradable Zn-1X binary alloys with nutrient alloying elements Mg, Ca and Sr.* Scientific Reports (Nature Publisher Group), 2015. **5**: p. 10719.

53. Murni, N.S., et al., *Cytotoxicity evaluation of biodegradable Zn–3Mg alloy toward normal human osteoblast cells.* Materials Science and Engineering: C, 2015. **49**: p. 560-566.

54. Bowen, P.K., J. Drelich, and J. Goldman, *Zinc Exhibits Ideal Physiological Corrosion Behavior for Bioabsorbable Stents.* Advanced materials (Weinheim), 2013. **25**(18): p. 2577-2582.

55. Han, P., et al., *Shape and site dependent in vivo degradation of Mg-Zn pins in rabbit femoral condyle.* International journal of molecular sciences, 2014. **15**(2): p. 2959-2970.

56. Yang, H., et al., *Evolution of the degradation mechanism of pure zinc stent in the one-year study of rabbit abdominal aorta model.* Biomaterials, 2017. **145**: p. 92-105.

57. Kandala, B.S.P.K., et al., *In Vitro and In Vivo Testing of Zinc as a Biodegradable Material for Stents Fabricated by Photo-Chemical Etching.* Applied sciences, 2019. **9**(21): p. 4503.

58. Yang, H., et al., *Alloying design of biodegradable zinc as promising bone implants for load-bearing applications.* Nature communications, 2020. **11**(1): p. 1-16.

59. Vojtěch, D., et al., *Mechanical and corrosion properties of newly developed biodegradable Zn-based alloys for bone fixation.* Acta Biomaterialia, 2011. **7**(9): p. 3515-3522.

60. Qin, Y., et al., *Additive manufacturing of biodegradable metals: Current research status and future perspectives.* Acta Biomaterialia, 2019.

61. Hong, S., et al., *Fabrication of 3D Printed Metal Structures by Use of High-Viscosity Cu Paste and a Screw Extruder.* Journal of Electronic Materials, 2015. **44**(3): p. 836-841.

62. Agrawal, R., et al., *Paste-based 3D printing of metallic materials: effect of binders and precursor sizes.* Materials Research Express, 2019. **6**(10).

63. Dini, F., et al., *A review of binder jet process parameters; powder, binder, printing and sintering condition.* Metal powder report, 2020. **75**(2): p. 95-100.

64. Mohd Amin Farhan, Z., et al., *Electrochemical Impedance Spectroscopy (EIS) Evaluation of Hydroxyapatite-Coated Magnesium in Different Corrosion Media.* Solid State Phenomena, 2018. **280**: p. 243-247.

65. Ha, H.-Y., et al., *Limitations in the use of the potentiodynamic polarisation curves to investigate the effect of Zn on the corrosion behaviour of as-extruded Mg–Zn binary alloy.* Corrosion Science, 2013. **75**: p. 426-433.

66. Shanmugam, S., et al., *Spectrophotometric analysis to monitor the corrosion behaviour of magnesium during immersion corrosion testing: A suitable alternative to pH measurement?* Corrosion Science, 2014. **89**: p. 338-342.

67. Kapsabelis, S. and C.A. Prestidge, *Adsorption of Ethyl(hydroxyethyl)cellulose onto Silica Particles: The Role of Surface Chemistry and Temperature.* Journal of Colloid and Interface Science, 2000. **228**(2): p. 297-305.

68. Lu, X., et al., *Solvent-based paste extrusion solid freeforming.* Journal of the European Ceramic Society, 2010. **30**(1): p. 1-10.

69. Sadighikia, S., S. Abdolhosseinzadeh, and H. Asgharzadeh, *Production of high porosity Zn foams by powder metallurgy method.* Powder Metallurgy, 2015. **58**(1): p. 61-66.

70. Sankaranarayanan, S. and M. Gupta, *Review on mechanical properties of magnesium (nano)composites developed using energy efficient microwaves.* Powder metallurgy, 2015. **58**(3): p. 183-192.

71. Instruments, G., *Getting Started With Your First Experiment.* 2021.

72. Abdalla, M.J., Alexander; Elahinia, Mohammad; Ibrahim, Hamdy, *Corrosion Modeling of Magnesium and Its Alloys for Biomedical Applications: Review.* Corrosion and Materials Degradation, 2020: p. 29.

73. Pan, Y., et al., *In vitro degradation and electrochemical corrosion evaluations of microarc oxidized pure Mg, Mg–Ca and Mg–Ca–Zn alloys for biomedical applications.* Materials Science and Engineering: C, 2015. **47**: p. 85-96.

APPENDIX A

EXPERIMENTAL DATA COLLECTION TABLES

Table A-1

Raw Data for Density Calculations of the Nanocomposites

Calculated Density of $MgSm_2O$ Nanocomposites							
	sample	D mm	t mm	V cm3	M g	rho g/cm3	Avg rho g/cm4
Pure	1	7.1	2.85	0.112837	0.184	1.63067114	1.607862224
	2	7	2	0.076969	0.122	1.58505331	
0.5	1	7.1	2.95	0.116796	0.194	1.6610134	1.662268161
	2	7.1	2.9	0.114817	0.191	1.66352293	
1	1	7.15	3.1	0.12447	0.206	1.6550212	1.663629148
	2	7.15	2.8	0.112424	0.188	1.67223709	
1.5	1	6.65	2.95	0.10246	0.18	1.75677975	1.75224226
	2	6.65	2.85	0.098987	0.173	1.74770477	

Table A-2

Raw Data for Measured Density of the Nanocomposites

Measured Density of $MgSm_2O$ Nanocomposites										
	Sample	r1	r2	r3	r4	r5	average/ sample	average	Theoretical	%porosity
Pure	1	1.890	1.714	1.595	1.754	1.832	1.7570	1.7255	1.73800	0.719217
	2	1.700	1.661	1.655	1.734	1.720	1.6940			
0.50%	1	1.767	1.647	1.722	1.722	1.722	1.7160	1.7160	1.77106	3.108873
	2	1.722	1.690	1.722	1.767	1.620	1.7042			
1%	1	1.827	1.827	1.763	1.763	1.687	1.7734	1.7749	1.81281	2.091229
	2	1.794	1.894	1.578	1.722	1.894	1.7764			
1.50%	1	1.631	1.883	1.794	1.994	1.794	1.8192	1.7901	1.85456	3.475757
	2	1.540	1.794	1.794	1.794	1.883	1.7610			

VITA

Austin Sims was born in Fort Oglethorpe, Georgia, to Mr. Randy and Mrs. Lynne Sims. He is the youngest in the family with an older sister who works in the biochemistry field. He attended Dade County Elementary and continued to Baylor High School in Chattanooga, Tennessee. After graduation, Austin attended Georgia Southern University where he became interested in the field of engineering. He completed a Bachelors of Science degree in Mechanical Engineering and Bachelors of Science degree in Nuclear Engineering from the University of Tennessee at Chattanooga. An interest in expanding his engineering education to the medical field led him to conduct research under Dr. Hamdy Ibrahim. Austin graduated from the University of Tennessee at Chattanooga with a Masters of Science degree in Mechanical Engineering in May 2021.